JᴍM PAPERS

Modulation of coaxial cone-jet instability in active co-flow focusing

Kai Mu[1], **Ran Qiao**[1], **Hang Ding**[1] **and Ting Si**[1],†

[1]Department of Modern Mechanics, University of Science and Technology of China, Hefei 230026, PR China

The breakup of coaxial cone-jet interfaces to compound droplets in axisymmetric co-flow focusing (CFF) upon actuation is studied through numerical simulations. Due to the coupling effect of double interfaces, the response behaviours of coaxial cone-jet flow to actuation are more complex than those of a single-layered interface structure. Particularly, the coaxial jet presents totally different response modes between weak and strong interface coupling situations. In this work, the phase diagrams of response modes for coaxial jet breakup are depicted, considering the effect of perturbation frequency, amplitude and liquid flow rates. In particular, the breakup of a coaxial jet can be synchronized with actuation within a frequency range containing the natural breakup frequency, resulting in uniform compound droplets with a single core inside the shell, and the size of droplets can be adjusted by frequency. As the perturbation frequency exceeds the upper critical value, the external perturbation is unable to dominate the jet breakup, while below the lower critical frequency, the jet breaks up with multiple droplets generated in one period. The perturbation amplitude mainly affects the jet breakup length and also leads to the transition between different response modes. The coaxial cone upstream of the orifice can act as a buffer layer, regulating the perturbation amplitude of the coaxial jet downstream. The degree of buffering effect is affected by the perturbation frequency and amplitude. As the perturbation amplitude approaches unity, the decrease of perturbation frequency leads to the intermittent jet behaviour from the cone tip with a vibrating manner of the coaxial cone. Based on the linear instability analysis on the simplified single jet models for weak-coupled and strong-coupled jets, scaling analyses are carried out, which predict the jet breakup length and the natural frequency and critical frequency for the synchronized breakup. Finally, a strong pulse is added on the perturbation to produce compound droplets with a controllable number of cores. The present work provides valuable guidance for the practical application of on-demand compound droplet generation through active CFF.

Key words: drops, jets, multiphase flow

† Email address for correspondence: tsi@ustc.edu.cn

K. Mu, R. Qiao, H. Ding and T. Si

1. Introduction

Microcapsules refer to the compound droplets with double-layered core-shell structures at micro scales, and have been widely applied in many industrial fields such as pharmaceutics, biology, chemistry, food industry and materials science (Vladisavljević, Nuumani & Nabavi 2017; Chen *et al.* 2021; Zhu & Wang 2022). In these applications, the compound droplets are usually required to have a large production rate, high encapsulation rate, controllable geometry and be suitable to different materials, which brings challenges to the preparation of compound droplets. The capillary flow method is a popular way to produce compound droplets, which is able to stretch the fluid interface to microscale purely through mechanical force (Barrero & Loscertales 2007; Anna 2016; Guerrero *et al.* 2020). Among the various configurations of capillary flow, one typical kind is called co-flow focusing (CFF) (Herrada *et al.* 2010; Gañán-Calvo *et al.* 2013). The configuration of CFF mainly comprises a coaxial capillary tube and a focusing orifice. In CFF the core and shell liquid flow through the coaxial tube and get focused by the continuous focusing fluid at the orifice. A converging coaxial cone forms upstream of the orifice and the coaxial jet forms downstream of the orifice in an unbounded environment. The disintegration of the coaxial jet further leads to the formation of the compound droplets. Compared with the single-axial flow focusing that has a mono-layered interface structure (Gañán-Calvo 1998; Herrada, Gañán-Calvo & Ojeda-Monge 2008), more complex interface morphologies can be observed for the double-layered coaxial cone and jet in CFF. Mechanical actuation has also been added to modulate the breakup of a coaxial liquid jet, realizing the on-demand generation of compound droplets (Bocanegra *et al.* 2005).

In CFF a stable coaxial cone is the precondition for the establishment of a coaxial liquid at the orifice downstream. Gañán-Calvo *et al.* (2007) studied the morphology of a coaxial liquid cone under different combinations of core and shell liquids. They found that the core droplets with diameters smaller than submicrometre can be formed when the flow rate of the core phase decreases close to the continuum limit, resulting in droplets with a much smaller size than those produced via single-axial flow focusing (Gañán-Calvo 1998). Based on the slender-body theory, Evangelio, Campo-Cortes & Gordillo (2016) predicted the interface profiles of the coaxial cone, which reached a good agreement with experimental results. Mu *et al.* (2022) carried out a comprehensive investigation on the morphology and instability of the coaxial cone in a triple-liquid system. It was observed that the liquid flow rates, viscosities, interfacial tensions and the geometrical parameters all have a significant influence on the cone instability, and the dimensional analysis was carried out to quantify the effect of these parameters. It is also found that under certain conditions, a recirculation flow occurs inside the inner liquid cone. The mechanism for the occurrence of recirculation flow can be attributed to the balance of shear force at both sides of the interface.

Under a stable coaxial cone, a coaxial liquid jet can emit from the cone tip and eventually breakup to a chain of compound droplets. Due to the interplay between the inner and outer jet interfaces, the coupling manner on the instability of double interfaces can be very complex, leading to more abundant breakup behaviours of the coaxial jet than those of the single jet (Gañán-Calvo & Riesco-Chueca 2006; Gañán-Calvo & Montanero 2009; Si *et al.* 2009; Mu, Ding & Si 2018*a*). In the experimental results of Herrada *et al.* (2010), it was observed that the relative flow rate between the inner and outer jets has a significant impact on the jet breakup characteristics, and the number of cores inside the shell droplets decreases with an increase of the inner flow rate. In order to study the interface coupling, Mu, Ding & Si (2020*a*) conducted a series of experiments in which the flow velocity and the outer diameter of the coaxial jet were kept constant, but the inner jet diameter was varied. It was found that at a small diameter ratio between the inner and outer jets, the

breakup of inner and outer jets was rather independent, suggesting a weak coupling manner between the double interfaces. However, at a relative large diameter ratio between inner and outer jets, the evolution of inner and outer jets was almost synchronized, indicating a strong coupling manner between double interfaces. Apart from experimental investigation, numerical simulations are also widely utilized to study the dynamic behaviours of a coaxial jet (Liu *et al.* 2017; Wang *et al.* 2020; Zhang *et al.* 2021). Numerical simulations can provide quantitative data such as the velocity field and pressure distribution of the jet, which are often difficult to measure in experiments.

Linear instability analysis is a powerful tool to investigate the breakup of liquid jets, which has developed considerably in the last hundred years (Eggers 1997; Lin 2003; Eggers & Villermaux 2008). For the coaxial jet, it has been found that the double interface exists in two typical perturbation modes, which are the in-phase stretching mode and the anti-phase squeezing mode (Chauhan *et al.* 2000; Chen & Lin 2002). The perturbation growth of the stretching mode was found to be faster than that of the squeezing mode, except at some extreme cases (Craster, Matar & Papageorgiou 2005). The physical mechanism for the dominance of the stretching mode over the squeezing mode can be explained as follows: the growth of interface perturbation on the inner jet gives rise to capillary pressure inside the outer jet, and the high pressure zone between the double interfaces leads to the in-phase perturbation of the coaxial jet (Mu *et al.* 2020*a*). Recently, a theoretical model of a coaxial liquid jet that considers the real flow field in CFF was developed (Mu, Li & Si 2020*b*). By comparing the perturbation growth rate between the coaxial jet model and the single jet models, the typical ranges of jet diameter ratio dividing the weak and strong interface coupling behaviours were obtained (Mu *et al.* 2020*b*).

Although CFF has been proven to be an efficient way to produce compound droplets, some non-negligible limitations also exist. For example, the breakup of the coaxial jet is not entirely periodic due to the random perturbation on the interface; therefore, the droplet size usually falls within some range, and satellite droplets always form with the main droplet. Moreover, it is very challenging to control the core-shell geometry of a compound droplet accurately. These shortcomings highlight the necessity for on-demand control of jet breakup and droplet production. Currently, the controlled breakup of a single jet falling into a stationary air environment has been widely studied, and the jet breakup has been successfully modulated by laser illumination (Liu *et al.* 2021; Zhao *et al.* 2021), a thermal field (Basaran, Gao & Bhat 2013; Kamis, Eral & Breugem 2021), electrical field (Yang *et al.* 2014; Xu *et al.* 2022*a*) and mechanical vibration (Moallemi, Li & Mehravaran 2016; She *et al.* 2022; Luo *et al.* 2023). As for the flow focusing system with an immiscible liquid phase, previous works by our group have considered the response of a liquid jet to an external periodic perturbation added to the flow rate, either through experiments (Yang *et al.* 2019) or numerical simulations (Mu *et al.* 2018*b*). When the frequency of the supplied actuation is close to the natural frequency of jet breakup, the liquid jet breaks up with the external actuation synchronously, and droplets with a uniform size can be generated. The forced jet breakup in a much faster driving air stream was also studied (Xu *et al.* 2022*b*). Compared with the liquid-driven situation, the gas-driven flow focusing leads to a much faster breakup frequency of the jet. Up to now, the investigation on the active modulation of the coaxial jet breakup is very limited. Bocanegra *et al.* (2005) applied sinusoidal excitation on both the inner and outer jet in a CFF system. As the frequency of the supplied actuation is very close to the natural frequency for the breakup of stretching perturbation, they realized the synchronized breakup of both the inner and outer jet with the excitation, resulting in uniform compound droplets with a single core inside. By adding a pulse every certain excitation period, they also realized the controllable number of cores

inside the droplets. However, a systematic study on the dynamics of coaxial jet breakup under external actuation is still desired, especially on the effect of perturbation frequency, amplitude and liquid flow rates on the response of jet breakup and the morphology of compound droplets. As the coaxial liquid cone upstream of the focusing orifice has a significant impact on the establishment and evolution of the coaxial jet, the dynamic behaviours of the coaxial cone under actuation also need to be studied in detail.

In this study we aim to study the dynamics of a coaxial liquid jet under periodic flow rate perturbation through numerical simulations. The paper is organized as follows. Section 2 introduces the numerical methods of CFF. Section 3 studies the response dynamics of the coaxial liquid cone under external actuation. In § 4 we investigate the response modes of jet breakup under different interface coupling situations, where the effects of perturbation frequency, amplitude and liquid flow rates are studied systematically. Theoretical analyses are provided in § 5. The controllable production of multi-core droplets is examined in § 6. Finally, main conclusions are given in § 7.

2. Numerical methods

We consider the CFF process with periodic modulated liquid flow rates at the inlet, as sketched in figure 1(*a*). The geometry mainly comprises a coaxial capillary tube (with length L) and a focusing orifice downstream, with distance H between them. In CFF the core liquid (with density ρ_1, dynamic viscosity μ_1, flow rate Q_1 and inlet velocity U_1) flows through the inner tube (with inner radius $0.5D_1$ and wall thickness T_1), coflowing with the shell liquid (with density ρ_2, dynamic viscosity μ_2, flow rate Q_2 and inlet velocity U_2) that flows through the outer tube (with inner radius $0.5D_2$ and wall thickness T_2). Then, the core and shell liquids get focused at the orifice (with radius $0.5d$ and thickness T) by a third phase of focusing liquid (with density ρ_3, dynamic viscosity μ_3, flow rate Q_3 and inlet velocity U_3). As a result, a coaxial liquid cone is established between the capillary tube and the orifice. Under certain conditions, the cone maintains stable and an axisymmetric coaxial liquid jet emits from the tip of the cone, evolves downstream of the orifice and ultimately breaks up into compound droplets due to interfacial instabilities. The geometric parameters are shown clearly in the amplified graph of the cone region in figure 1(*b*). It has been proved that in a wide range of geometric parameters, the coaxial liquid cone can maintain stable, and the geometric parameters only have an insignificant effect on the breakup of the coaxial liquid jet downstream of the orifice (Mu *et al.* 2022). Therefore, the geometric parameters are chosen moderately and kept constant in our work. The liquids are chosen as a water-in-oil-in-water system, which is the same as considered in our previous studies (Mu *et al.* 2020*a*, 2021*b*). Therefore, the coaxial cone-jet flow corresponds to a two-phase liquid system (i.e. $\rho_1 = \rho_3$, $\mu_1 = \mu_3$). The interfacial tension coefficient between the water and oil phase is denoted by σ. It is notable that the two-phase system has been widely applied in real experiments for producing double emulsions (Evangelio *et al.* 2016; Liu *et al.* 2020).

In numerical simulations, the actuation can be imposed on the inlet of the supplied liquids through prescribing the time-dependent flow rates. We mainly focus on the situation where synchronous actuations with a sinusoidal waveform are imposed on the core and shell liquid, as shown in figure 1(*c*). Meanwhile, the flow rate of the focusing liquid keeps constant. Under these conditions, the inlet velocity U_3 maintains a constant value, while $U_1(t)$ and $U_2(t)$ fluctuate sinusoidally with identical amplitude and frequency, i.e.

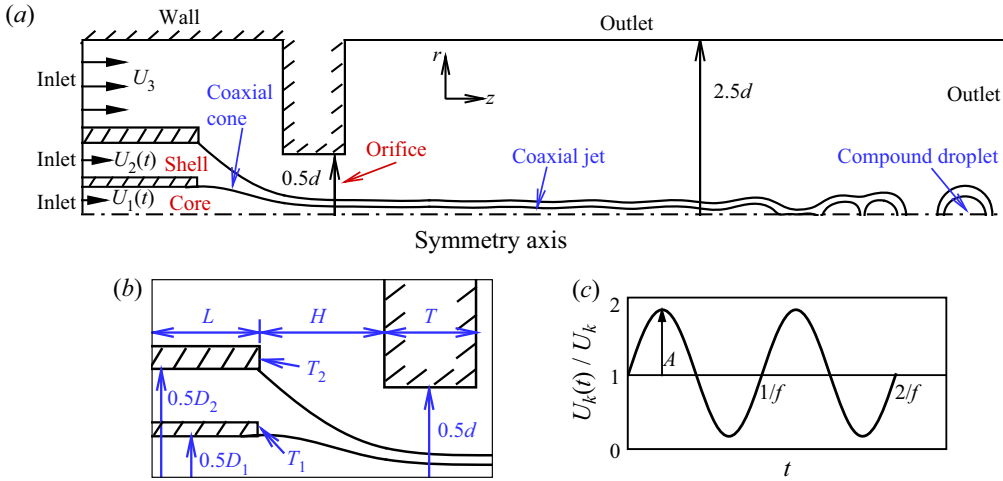$$U_1(t) = U_1(1 + A\sin(2\pi ft)) \quad \text{and} \quad U_2(t) = U_2(1 + A\sin(2\pi ft)), \qquad (2.1a,b)$$

Figure 1. (*a*) Axisymmetric computational domain for numerical simulations, where $U_1(t)$, $U_2(t)$ and U_3 stand for the inlet velocities of the core, shell and focusing liquids, respectively. (*b*) Sketch of the geometrical parameters. (*c*) Temporal evolution of dimensionless inlet velocities, where $k = 1, 2$ for $U_k(t)$ and U_k.

where A and f stand for the dimensionless amplitude and frequency of perturbations, respectively. It is notable that, for producing compound droplets with controllable cores, we consider the situation of applying a strong pulse on the liquid flow rate every certain number of periods, which will be shown in a later section.

In numerical simulations a diffuse interface method is applied to differentiate the two-phase liquids. In this method, the liquid interface is represented by a volume fraction C, which varies continuously from the value 1 to 0 across the interface. The finite thickness characteristic of the liquid interface can avoid the stress singularity, resulting in a more accurate calculation on the interfacial tension force compared with the sharp interface method such as level set or volume of fluid (Ding, Spelt & Shu 2007). This point is very vital for the numerical simulation of CFF as the generation of compound droplets is dominated by the interfacial tension. The evolution of the interface is governed by the convective Cahn–Hillard equation (Jacqmin 1999),

$$\frac{\partial C}{\partial t} + \nabla \cdot (\boldsymbol{u}C) = \frac{1}{Pe}\nabla^2 \Psi, \tag{2.2}$$

where Pe is the Péclet number, and the chemical potential Ψ is defined as

$$\Psi = C^3 - 1.5C^2 + 0.5C - Cn^2\nabla^2 C, \tag{2.3}$$

in which the Cahn number Cn measures the thickness of the diffuse interface. Generally, Cn is selected to be $Cn \sim \Delta x$ in order to better resolve the diffusion interface and ensure an accurate surface tension calculation, where Δx is the mesh size. A larger value of Cn results in a thicker diffuse interface but a more accurate calculation of the surface tension force, due to the fact that more meshes resolve the interface. Based on our previous experience (Mu *et al.* 2018*b*; Mu, Si & Ding 2019; Mu *et al.* 2021*a*), we set $Cn = 0.5\Delta x$. The Péclet number Pe represents the relative significance of convective fluxes to the diffusive fluxes. As suggested in Magaletti *et al.* (2013), the diffuse interface approaches the sharp interface limit with the vanishing of Cn for $Pe \sim Cn^{-1}$. Therefore, we adopt $Pe = 1/Cn$ in the present study.

The motion of fluids is governed by the dimensionless Navier–Stokes equations, i.e.

$$\rho \left(\frac{\partial \boldsymbol{u}}{\partial t} + \boldsymbol{u} \cdot \nabla \boldsymbol{u} \right) = -\nabla p + \frac{1}{Re} \nabla \cdot [\mu (\nabla \boldsymbol{u} + \nabla \boldsymbol{u}^T)] + \frac{\boldsymbol{f}_s}{We}, \tag{2.4}$$

$$\nabla \cdot \boldsymbol{u} = 0, \tag{2.5}$$

where $\boldsymbol{f}_s = 6\sqrt{2}\Psi \nabla C/Cn$ denotes the surface tension force, $\rho = C + (1 - C)r_\rho$ and $\mu = C + (1 - C)r_\mu$ are the dimensionless averaged density and viscosity, $r_\rho = \rho_2/\rho_1$ and $r_\mu = \mu_2/\mu_1$ are the density and viscosity ratios between different phases of liquids, respectively. Choosing the core and focusing liquids as the characteristic phase, D_2 as the characteristic length and U_3 as the characteristic velocity, the Reynolds and Weber numbers in (2.4) can be defined as $Re = \rho_1 U_3 D_2/\mu_1$ and $We = \rho_1 U_3^2 D_2/\sigma$. The characteristic time and frequency correspond to D_2/U_3 and U_3/D_2, respectively. As the variation of U_3 will change the values of Re and We simultaneously, we also define the Ohnesorge number as $Oh = \mu_1/\sqrt{\rho_1 \sigma D_2}$ for the convenience of analysis. In addition, we define the flow rate ratios $r_{Q1} = Q_1/Q_3$ and $r_{Q2} = Q_2/Q_3$ to quantify the relative flow rates of the core and shell liquids with respect to the focusing liquid, respectively.

The numerical simulations are performed in the $r - z$ cylindrical coordinate on a uniform Cartesian mesh, where r and z denote the radial and axial directions, respectively. The computational domain is set as $2D_2 \times 10D_2$, which is long enough to resolve the liquid jet evolution until its breakup. The mesh size is $\Delta x = 0.002D_2$, which is fine enough to resolve the coaxial liquid jet and the compound droplets (e.g. the smallest diameter of the inner jet or droplets is about $0.07D_2$). The interface is represented by the $C = 0.5$ contour. The boundary conditions for the flow velocities are given as follows: $v = 0$, $\partial u/\partial r = 0$ at the axis of symmetry $r = 0$, where u and v are the flow velocities at r and z directions, respectively; no-slip condition at the solid wall ($u = v = 0$); $\partial u/\partial z = 0$ and $\partial v/\partial t + v \cdot (\partial v/\partial z) = 0$ at the rightside outlet; $\partial v/\partial r = 0$ and $\partial u/\partial t + u \cdot (\partial u/\partial r) = 0$ at the upperside outlet; $U = U_k$ ($k = 1, 2, 3$) and $v = 0$ at the inlet, where U_k is a prescribed value according to the flow rate.

The parameters chosen for numerical simulations correspond to our previous experimental set-up without flow rate actuation (Mu *et al.* 2020a, 2021b, 2022), where the core and focusing liquids are chosen as the distilled water ($\rho_1 = \rho_3 = 996$ kg m^{-3} and $\mu_1 = \mu_3 = 0.001$ Pa s), and the shell liquid is chosen as silicone oil with constant dynamic viscosity ($\rho_2 = 965$ kg m^{-3} and $\mu_2 = 0.04$ Pa s). The interfacial tension coefficient between water and silicone oil is $\sigma = 32.8$ mN m^{-1}. The geometrical parameters are $D_2 = 1050$ μm, $D_1 = 420$ μm, $d = 840$ μm, $H = 630$ μm and $T = 420$ μm, respectively. Therefore, the density and viscosity ratios are constant at $r_\rho = 0.97$ and $r_\mu = 40$, and the Ohnesorge number keeps constant at $Oh = 0.005$. The geometrical parameters are set at $D_1 = 0.4D_2$, $d = 0.8D_2$, $H = 0.6D_2$, $T = 0.4D_2$, $T_1 = 0.02D_2$, $T_2 = 0.1D_2$ and $L = D_2$, respectively. It is pointed out that the tube length L is demonstrated to be sufficiently long in simulations, ensuring that the liquid velocity profiles in the capillary tube can develop into the steady pipe flow ones quickly. The Reynolds number Re varies with the flow rate Q_3 of the focusing liquid. In this work, the values of Q_3 vary within 1150 and 2100 ml h^{-1}, corresponding to the change of Re from 27.9 to 49.1. The experimental results within this parameter range have shown that the coaxial liquid jets maintain the axisymmetric evolution without occurrence of non-axisymmetric perturbation (Mu *et al.* 2020a, 2021b). The numerical code has been carefully validated by experiments reported in previous studies (Mu *et al.* 2020a, 2021b, 2022), where good agreements of the coaxial cone-jet interface profiles and the generation of compound droplets can be reached.

977 A14-6

3. Dynamics of coaxial liquid cone

We firstly consider the response dynamics of the coaxial liquid cone upon external actuation as it is closely related to the behaviours of jet breakup and droplet generation downstream of the orifice. In this section we examine the evolution of the coaxial cone under different perturbation amplitudes A and frequencies f and also elucidate the mechanism of unstable cone-jet flow at specific parameter regions. It has been observed in our previous work that the flow field inside the coaxial liquid cone can be totally different as the flow rate of core liquid varies (Mu *et al.* 2022). Specifically, the recirculation flow occurs under a relatively low flow rate of core liquid. For the coaxial jet establishing at the coaxial cone tip, it has been found that the flow rate between the inner jet and the coaxial jets (defined as r_Q $(= r_{Q1}/(r_{Q1} + r_{Q2}))$) decides the jet diameter ratio κ and, thus, the coupling manner of the inner and outer interfaces, which further determines the final geometrical configuration of compound droplets (Mu *et al.* 2020*a*). The relationship between the jet diameter ratio and the flow rate ratio can be approximated as $\kappa \approx r_Q^{1/2}$. Without loss of generality, we mainly focus on the coaxial cone-jet flow at $r_Q = 0.5$ and $r_Q = 0.1$, under fixed values of $Re = 32.7$ and $r_{Q1} + r_{Q2} = 0.0714$, corresponding to the dimensional situation of $Q_3 = 1400$ ml h^{-1} and $Q_1 + Q_2 = 100$ ml h^{-1}, respectively. In these conditions, the characteristic velocity is $U_3 = 0.03$ m s^{-1}, which corresponds to a characteristic frequency of 28.5 Hz.

Figure 2(*a*) shows the dynamic evolution of the coaxial liquid cone at $r_Q = 0.5$ at two instants during the pulsation period, where the vorticity and pressure fields are presented in the upper and lower parts of each graph, respectively. The perturbation amplitude and frequency are given moderately as $A = 0.4$ and $f = 20$, and the coaxial cone is established upstream of the orifice, with its tip emitting the liquid jet downstream. For the axisymmetric flow in the *r–z* plane, the vorticity exists in the circumferential direction (denoted by θ) and has a magnitude equal to $\partial v/\partial r - \partial u/\partial z$, where u and v denote the velocity component at z and r coordinates, respectively. Compared with the situation of pure CFF where the liquid flow rates maintain constant values (Mu *et al.* 2022), the addition of external perturbations lead to a temporal pulsating pressure and vorticity field. For the core, shell and focusing liquids, the values of pressure gradually decrease as the flow evolves downstream due to the acceleration of the liquids. The presence of interfacial tension leads to a discontinuity of the pressure values across the interfaces. Perpendicular to the interfaces, the pressure value decreases from the core liquid to the shell liquid and to the focusing liquid. As for the vorticity field, the extreme values occur either close to the outer cone interface at the focusing orifice or close to the solid wall of the orifice, where the magnitude and direction of flow velocity change abruptly. This indicates that the quick stretching and deformation of the liquid interfaces at the orifice will cause a large gradient of the local velocity.

Figure 2(*b,c*) shows the temporal evolutions of the liquid flow rate and volume of the cone for the core and shell liquids, respectively. In these figures, $Q_k(t)$ and $Q_{kj}(t)$ represent the supplied flow rate at the capillary tube and the instant jet flow rate measured at the exit of the orifice, respectively. The average flow rate is denoted as $\bar{Q}_k$, and V_{kc} represents the cone volume measured from the capillary tube to the orifice exit, where $k = 1, 2$ represents the core liquid and the shell liquid, respectively. The two instants in figure 2(*a*) are also indicated in figure 2(*b,c*), corresponding to the moments with the minimum and maximum cone volumes. It is observed that the liquid cone acts as a reservoir for the downstream jet. Therefore, the perturbation amplitude of the jet is smaller than the flow rate amplitude applied from the capillary tube, whether for the inner or the outer cone. Furthermore,
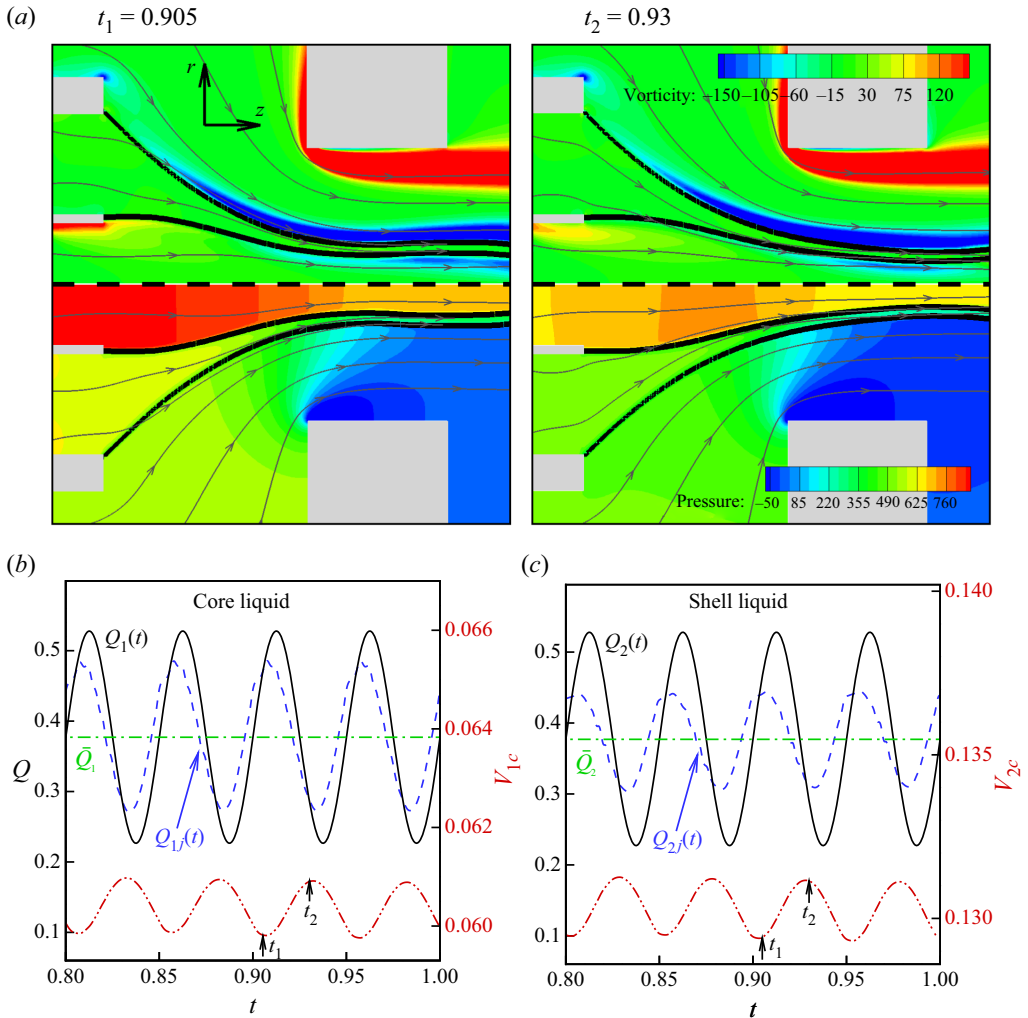
Figure 2. Evolutions of a coaxial liquid cone at $A = 0.4$, $f = 20$ and $r_Q = 0.5$, where $Re = 32.7$ and $r_{Q1} + r_{Q2} = 0.0714$. (*a*) Interface profiles and streamlines of a coaxial cone at two instants (denoted by t_1 and t_2) during the pulsation period, the contour at the upper and the lower half of each graph shows the vorticity and pressure field, respectively. (*b*) Temporal evolutions on the flow rate of core liquid measured at the capillary tube ($Q_1(t)$) and the inner jet at the orifice exit ($Q_{1j}(t)$) and the volume of the inner cone (V_{1c}). (*c*) Temporal evolutions on the flow rate of shell liquid measured at the capillary tube ($Q_2(t)$) and outer jet at the orifice exit ($Q_{2j}(t)$) and the volume of the outer cone (V_{2c}). The time instants t_1 and t_2 are also marked in (*b*) and (*c*).

the volume of the cone vibrates periodically. When $Q_k(t)$ is larger than $Q_{kj}(t)$, the cone volume increases to absorb the extra liquid. Conversely, as $Q_k(t)$ becomes smaller than $Q_{kj}(t)$, the cone volume decreases to release the liquid stored inside. Thus, the variation of cone volumes serves as a reservoir and enables the buffering of liquid flow rates.

The buffering effect of the liquid cone is significantly influenced by the amplitude A and frequency f of perturbations, as shown in figure 3(*a*,*b*), respectively. We have measured the amplitude of perturbation on jet flow rate, denoted as A_{kj} ($k = 1, 2$), by computing the difference between the maximum value of $Q_{kj}(t)$ and the average value $\bar{Q}_k$, i.e. $A_{kj} = (\max[Q_{kj}(t)] - \bar{Q}_k)/\bar{Q}_k$. In figure 3(*a*) both A_{1j} and A_{2j} show an approximately
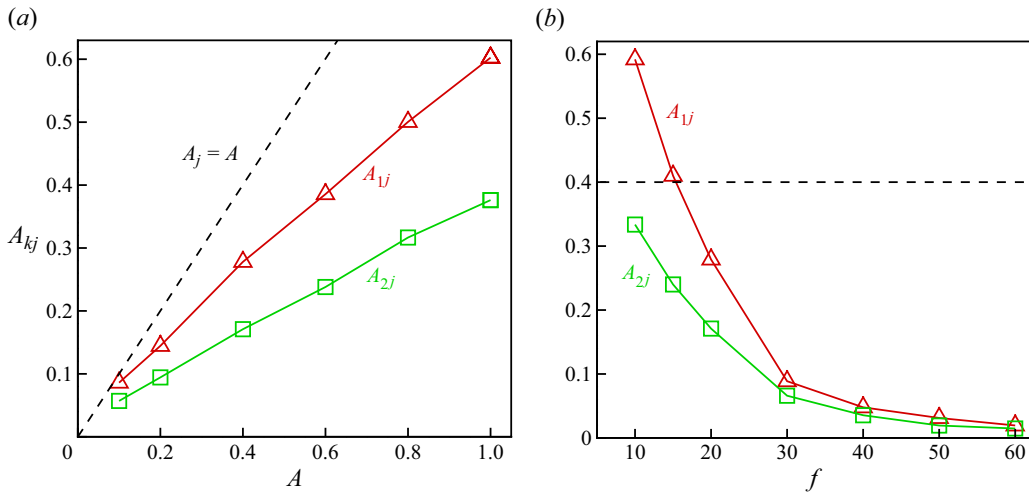
(*a*)

(*b*)

Figure 3. Perturbation amplitude of the pulsating flow rate of the inner and outer jet (denoted by A_{1j} and A_{2j}, respectively) as (*a*) A varies at $f = 20$ and (*b*) f varies at $A = 0.4$, under $r_Q = 0.5$. The dashed line denotes $A_j = A$.

linear increase with A. Notably, for a constant value of A, A_{1j} is observed to be larger than A_{2j}. This can be qualitatively explained by considering that the average volume of the inner cone is smaller than that of the outer cone (see figure 2*b*,*c*), leading to weaker damping of external oscillations in the inner cone and, thus, a larger perturbation amplitude of the inner jet. Figure 3(*b*) reveals that as f decreases, both A_{1j} and A_{2j} increase. The underlying reason is that a smaller f leads to a larger perturbation period, which brings in more extra liquid during the half-cycle of one perturbation period. Particularly, at relatively low f, A_{1j} can even exceed the amplitude of the supplied flow rate A, suggesting that the cone can promote the flow rate perturbation at the downstream jet.

Figure 4 presents the dynamic evolution of the coaxial cone at $r_Q = 0.1$, where the upper and lower parts of the graph show the vorticity and pressure fields, respectively. The perturbation amplitude and frequency are chosen to be moderate ($A = 0.4$ and $f = 20$) to ensure the formation of the coaxial cone-jet structure. Similar to the case of $r_Q = 0.5$, the addition of external perturbation causes a pulsating pressure and vorticity field in one period. The overall tendency for the evolutions of pressure and vorticity is also very similar to the case $r_Q = 0.5$. However, in contrast to the case $r_Q = 0.5$, a recirculation cell (RC) exists inside the inner liquid cone when $r_Q = 0.1$, and the evolution of streamlines is totally different. The occurrence of RC results in the backflow characteristic where the flow direction at the symmetry axis is opposite to that in the capillary tube. The mechanism for the occurrence of RC under relatively low flow rate of the inner core has been analysed in our previous work, which can be attributed to the balance of shear force at both sides of the interface (Mu *et al.* 2022). At a relatively low flow rate of the core liquid, the tangential velocity inside the interface of the inner cone decreases rapidly along the vertical direction and reverses some distance away from the interface, thus causing the occurrence of RC. However, at a large flow rate of the core liquid, the tangential velocity inside the interface of the inner cone maintains downstream consistently, and no RC occurs. Different from the situation of constant flow rate where the RC maintains a constant size, the addition of external perturbation to liquid flow rate leads to periodic changes in the length of RC (L_r), as shown in figure 4(*b*). The temporal variation on the RC length suggests the exchange of
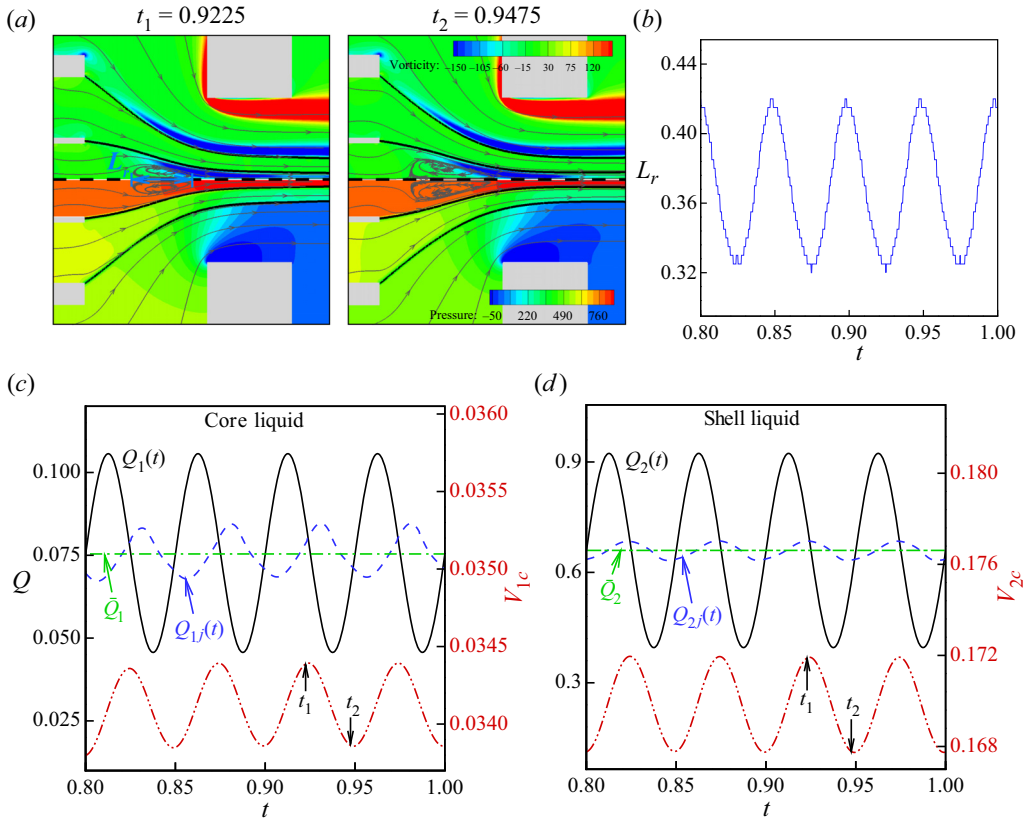
Figure 4. Evolutions of a coaxial liquid cone at $A = 0.4$, $f = 20$ and $r_Q = 0.1$, where $Re = 32.7$ and $r_{Q1} + r_{Q2} = 0.0714$. (a) Interface profiles and streamlines of a coaxial cone at two time instants (denoted by t_1 and t_2), the contour at the upper and the lower half of each graph shows the vorticity and pressure field, respectively. (b) Temporal variation of recirculation length L_r. (c) Temporal evolutions on the flow rate of core liquid measured at the capillary tube ($Q_1(t)$) and the inner jet at the orifice exit ($Q_{1j}(t)$) and the volume of the inner cone (V_{1c}). (d) Temporal evolutions on the flow rate of shell liquid measured at the capillary tube ($Q_2(t)$) and the outer jet at the orifice exit ($Q_{2j}(t)$) and the volume of the outer cone (V_{2c}). The time instants t_1 and t_2 are also marked in (c) and (d).

substance between the RC and the external liquid. The temporal evolutions of the liquid flow rate and volume of the cone are presented in figure 4(c,d) for the core and shell liquids, respectively. Similar to figure 2, $Q_k(t)$ and $Q_{kj}(t)$ represent the flow rates at the capillary tube and the jet flow rate at the exit of the orifice, $\bar{Q}_k$ represents the average flow rate and V_{kc} represents the cone volume, respectively. In the figures, $k = 1$, 2 represent the core and shell liquids, respectively. The two instants in figure 4(a) are indicated in figure 4(c,d), showing that the size of RC is directly related to the volume of the cone. Similarly, the reservoir effect of the liquid cone decreases the perturbation amplitude of the jet ($Q_{kj}(t)$) significantly compared with that of the capillary tube ($Q_k(t)$), and the volume of the cone varies periodically.

Figure 5 illustrates the degree of buffering effect provided by the liquid cone. The magnitudes of the perturbation amplitudes A_{1j} and A_{2j} are found to be significantly influenced by the perturbation amplitude A and frequency f. Specifically, both A_{1j} and A_{2j} present an approximately linear increase with A, as depicted in figure 5(a). For a given value of A, the value of A_{1j} is greater than that of A_{2j} due to the larger volume of the
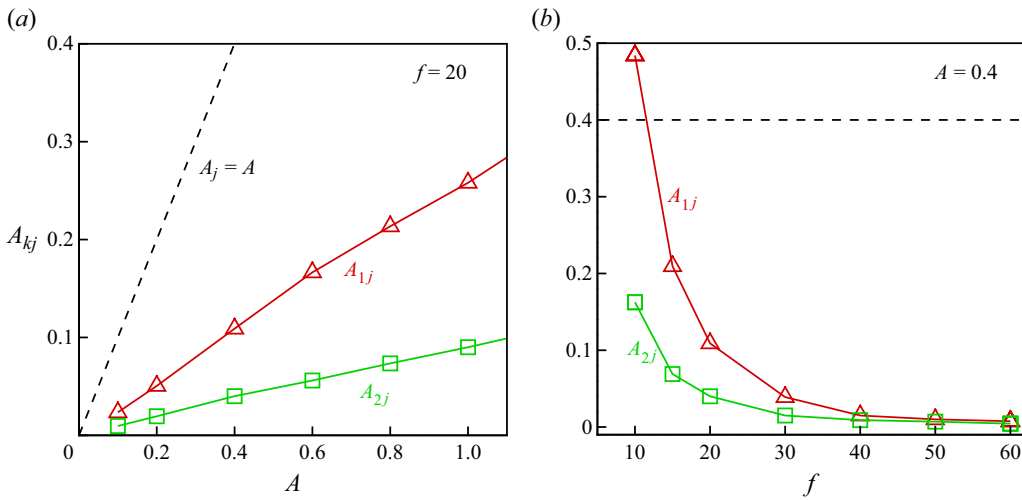
977 A14-10

Figure 5. Perturbation amplitude of the pulsating flow rate of the inner and outer jet (denoted by A_{1j} and A_{2j}, respectively) as (*a*) A varies at $f = 20$ and (*b*) f varies at $A = 0.4$, under $r_Q = 0.1$. The dashed line denotes $A_j = A$.

outer cone and its superior ability to damp the external perturbation. Moreover, figure 5(*b*) reveals that both A_{1j} and A_{2j} increase as f decreases. At relatively low values of f, the perturbation amplitude of the local liquid jet can even exceed that of the capillary tube.

As a larger A and a smaller f can lead to larger values of A_{1j} and A_{2j}, the external perturbation is supposed to have significant influence on the instability of the coaxial cone and jet at the parameter region of large A and small f. Figure 6 shows the dynamical behaviours of an unstable cone-jet structure at $A = 1$ and $f = 5$, with $r_Q = 0.5$ in figure (*a*) and $r_Q = 0.1$ in figure (*b*), respectively. As we have learned from figures 3(*b*) and 5(*b*), a smaller f (e.g. $f \leq 10$) can result in a larger pulsation amplitude of the jet than the amplitude of the flow rate at the capillary tube, especially for the inner jet. Therefore, the flow rate of the inner jet is able to evolve to zero for the perturbation amplitude $A = 1$, causing the stagnation of downstream flow at the local jet and the destabilization of the liquid jet. We also give the temporal evolutions of the inner jet flow rate $Q_{1j}(t)$ with the flow rate $Q_1(t)$ from the capillary tube in figure 6(*c,d*), respectively. Compared with the situation where the jet establishes downstream of the orifice (see figures 2 and 4), the flow dynamics is modulated significantly under relatively large A and small f. As the jet emits from the cone and evolves downstream, $Q_1(t)$ first reaches the maximum value and then decreases rapidly due to the continuous thinning of the jet (e.g. $t = 0.8$). As the jet pinches off at the cone tip, the inner cone recoils to the orifice upstream (e.g. $t = 0.86$). The unsteady flow characteristics of the cone also leads to intermittent occurrence of the RC inside the cone, as shown by the streamlines in figure 6(*a,b*), respectively. The dynamics of the outer jet is a bit different as r_Q changes. For the case $r_Q = 0.5$, the breakup of the inner liquid will cause a synchronous breakup of the outer interface due to the strong coupling effect of double interfaces; therefore, the outer interface also presents the intermittent jet behaviour and recoils upstream of the orifice after breakup. For the case $r_Q = 0.1$, as the interplay between the inner and outer interface is relatively weak due to the large distance between them, the breakup of the inner interface of droplets can cause some bulges for the outer jet.
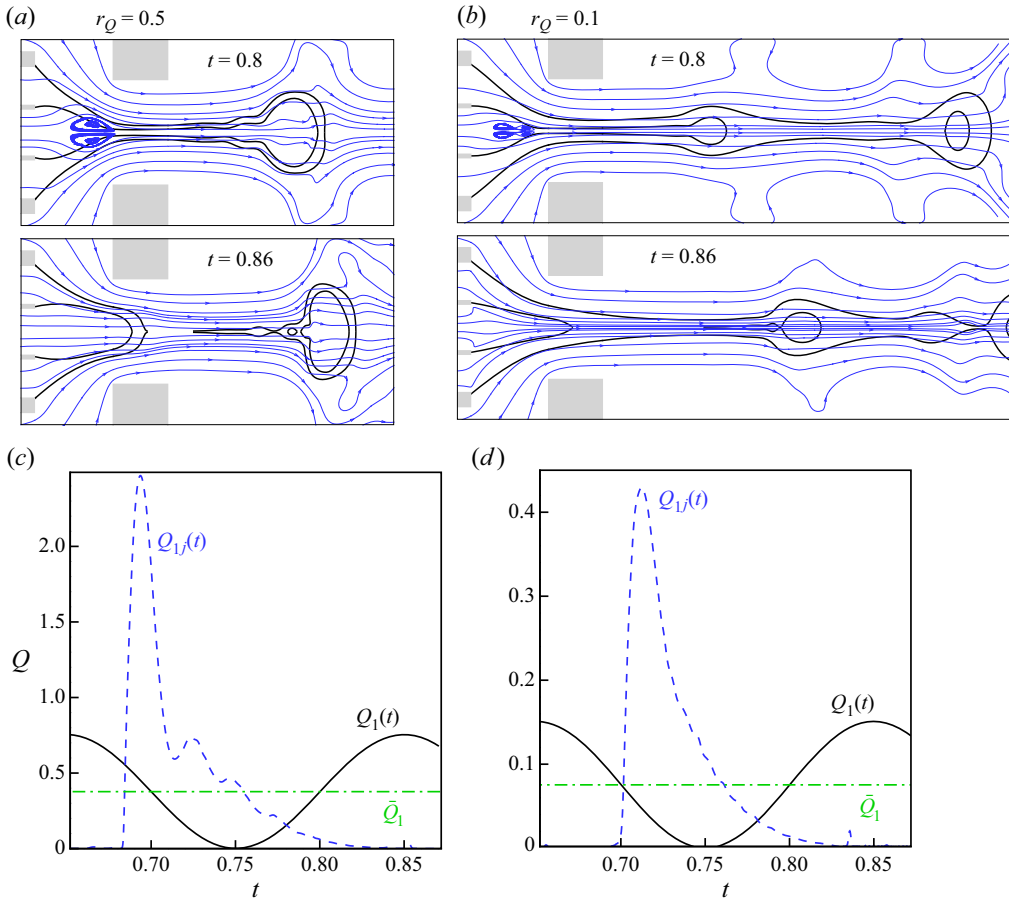
Figure 6. Dynamics of an unstable jet with a vibrating liquid cone at $A = 1$ and $f = 5$, where (*a*) $r_Q = 0.5$ and (*b*) $r_Q = 0.1$. Temporal evolutions on the flow rate of core liquid measured at the capillary tube (denoted by $Q_1(t)$) and the orifice exit (denoted by $Q_{1j}(t)$), where (*c*) $r_Q = 0.5$ and (*d*) $r_Q = 0.1$.

4. Response modes of coaxial liquid jet

In this section we focus on the response dynamics of coaxial liquid jets under different interface coupling situations. Our previous work (Mu *et al.* 2020*a*,*b*) indicated that for a weak-coupled jet at relatively low r_Q (or κ), the inner and outer liquid jets breakup almost independently, similar to two single liquid jets. As the coaxial liquid jets evolve and breakup, the compound droplets with multiple cores inside a shell can be formed. While for a strong-coupled jet at relatively high r_Q (or κ), the inner and outer liquid jets almost breakup synchronously, forming compound droplets with a single core inside. The typical parameter regions for weak-coupled and strong-coupled jets have been identified as $r_Q \leq 0.15$ and $r_Q \geq 0.4$, respectively. In this work, external actuations are brought in and the response dynamics of a strong-coupled jet at $r_Q = 0.5$ and a weak-coupled jet at $r_Q = 0.1$ are considered, respectively.

4.1. *Phase diagram*

When external actuation is applied to the flow, the behaviour of coaxial jet breakup is closely related to the frequency f and amplitude A of the perturbations. Figure 7(*a*)
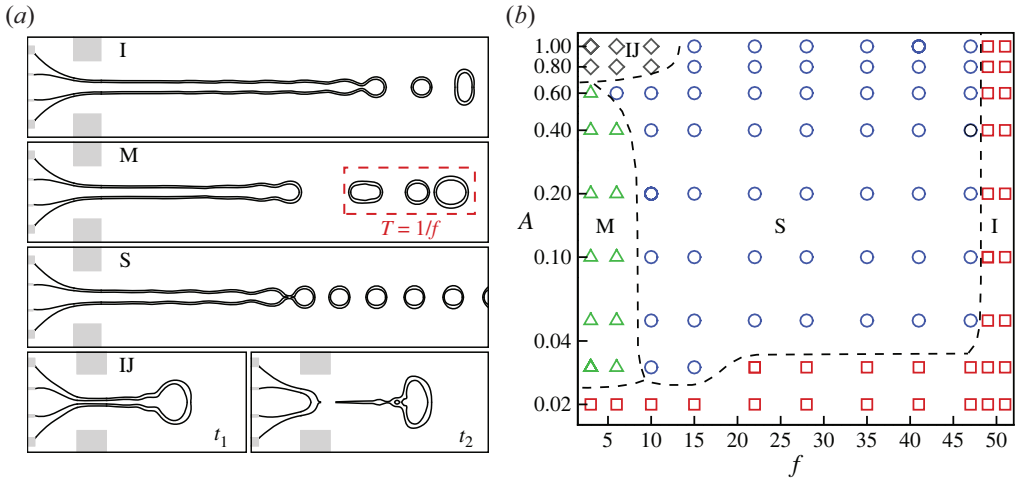
Figure 7. (*a*) Four typical response modes of jet breakup for a strong-coupled jet at $r_Q = 0.5$, where $Re = 32.7$ and $r_{Q1} + r_{Q2} = 0.0714$. The letter symbols I, M, S and IJ stand for the irregular breakup mode, the multiple breakup mode, the synchronized breakup mode and the intermittent jet mode, respectively. The dashed box contains the droplets generated in one period of $1/f$. (*b*) Phase diagram of the response modes as the values of f and A vary. The dashed lines denote the boundaries of different modes roughly.

shows the typical response modes of jet breakup for a strong-coupled jet at $r_Q = 0.5$. The corresponding phase diagram for different response modes as f and A vary is presented in figure 7(*b*). For the first type of response modes, the coaxial jet breakup is random without obvious periodicity, resulting in compound droplets within a certain size range. This mode is defined as the irregular breakup mode ('I' mode). It is notable that for the coaxial jet without actuation, the breakup exhibits the same as the I mode due to the random growth of perturbation. The second type of response modes corresponds to droplet generation with multiple sizes in a periodic manner, with the working period for the droplet series equal to $1/f$, which is defined as the multiple breakup mode ('M' mode). For the third type of jet breakup, the droplet generation is entirely synchronized with the imposed excitation, resulting in droplets with uniform size, which is defined as the 'S' mode. For the fourth type of response modes, the coaxial cone is unstable and vibrates periodically as the intermittent jet breaks at the cone tip, and the cone recoils to the orifice upstream accompanying with the droplet formation. This mode is defined as the intermittent jet ('IJ') mode. The phase diagram of different response modes for the strong-coupled jet is shown in figure 7(*b*). It is observed that there exists a critical value of A below which the jet breakup presents an I mode. Below the critical amplitude, the external actuation is too weak to affect the jet breakup. For moderate values of A (e.g. $A \geq 0.05$), there is a frequency range in which the S mode occurs, and the lower boundary of this frequency range decreases with A increasing while the upper boundary remains relatively constant. The wide frequency range of the S mode leads to a well adjustability of droplet generation with uniform size, which is favourable in real applications. Below this frequency range, the jet presents the M mode; while beyond this frequency range, the jet presents the I mode. The IJ mode region exists at large values of A and small values of f (e.g. $A \geq 0.8$ and $f \leq 10$).

The response modes of coaxial jet breakup under different f and A are much more complex for a weak-coupled jet than for a strong-coupled jet, since the inner and outer jets breakup asynchronously. Figure 8(*a*) shows the typical response modes of jet breakup

for a weak-coupled jet at $r_Q = 0.1$, and the corresponding phase diagram for different response modes is given in figure 8(*b*). The first response mode is the 'I-I' mode, where both the inner and outer jets breakup in a rather irregular manner, resulting in multiple core droplets inside a shell. It is notable that the core droplets tend to merge together due to the interplay of the diffuse interface in numerical simulations. However, this merging behaviour does not prevent us from counting the number of cores inside a compound droplet. The second response mode is the 'M-M' mode, where both the inner and outer jets breakup with multiple droplets in a working period $1/f$, resulting in droplets with non-uniform size. The third response mode corresponds to the 'M-S' mode, where the inner jet presents the M mode while the outer jet breaks synchronously with actuation (S mode). In this mode, compound droplets with uniform size and multi-cores inside can be generated. The fourth response mode is the 'S-S' mode, in which both the inner and outer jets breakup synchronously with the actuation. Consequently, compound droplets with single core inside a shell can be generated periodically. The fifth response mode is the 'S-I' mode. In this mode, the formation of inner droplets is synchronized with actuation, resulting in droplets of uniform size. Meanwhile, the outer jet breaks in a rather random manner, producing non-uniform size compound droplets. The last response mode is the intermittent jet ('IJ') mode, in which the dynamic behaviours of the coaxial cone and jet are similar to the strong-coupled case. The phase diagram of different response modes for the weak-coupled jet is shown in figure 8(*b*). There exists a critical value of A below which the jet breakup presents the I-I mode, indicating that the external actuation cannot modulate the jet breakup at very low amplitude. At a large value of A and small value of f (e.g. $A \geq 0.8$ and $f \leq 10$), the coaxial jet presents the IJ mode. The response for the coaxial jet breakup is much more complicated at moderate A. As f increases from very low values, the jet breakup presents the M-M mode and gradually transitions to the M-S, S-S, S-I and I-I modes. Specifically, the upper boundary for the synchronized frequency region is almost unaffected by A, while the lower boundary decreases with A increasing, both for the inner and outer jets.

4.2. *Effect of actuation frequency*

Figure 9(*a*) depicts the effect of actuation frequency f on the breakup of the strong-coupled jet ($r_Q = 0.5$) under constant perturbation amplitude $A = 0.1$. The variation of the corresponding diameter of compound droplets D_o changing with f is shown in figure 9(*b*). As the inner and outer jets evolve synchronously and eventually breakup into single core droplets, the diameters of core droplets can be predicted approximately through volume conservation, i.e. $D_i \approx r_Q^{1/3} D_o$. For an unexcited jet with $f = 0$, the breakup of the coaxial jet is rather random without periodicity, presenting the I mode, with the compound droplet sizes falling within a certain range. The average breakup frequency (also known as natural frequency, f_n) can be obtained by counting the number of droplets (denoted by N) in a long time sequence (denoted by T), which is $f_n = N/T$ and approximately equal to 23.5 in numerical simulations. The corresponding average droplets diameter is about 0.393. When the frequency increases to a relatively low value ($f = 6$), the coaxial jet breakup shifts to the M mode, where droplets with multiple discrete values of diameters are generated during a working period of $1/f$. A continuous increase of f leads to the S mode of jet breakup, which results in a droplet size. In this mode, the size and frequency of droplet generation can be effectively adjusted by varying f. Notably, the natural frequency f_n falls within the frequency range of the S mode. If f exceeds a critical value, the periodicity disappears, and the droplet generation becomes
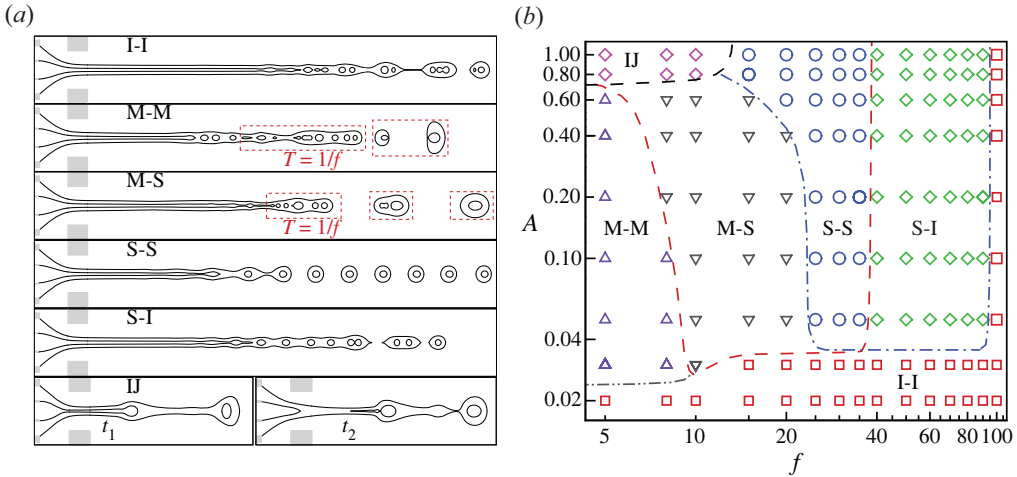
Figure 8. (*a*) Six typical response modes of jet breakup for a weak-coupled jet at $r_Q = 0.1$, where $Re = 32.7$ and $r_{Q1} + r_{Q2} = 0.0714$. The letter symbols I-I, M-M, M-S, S-S, S-I and IJ stand for the inner and outer irregular breakup mode, the inner and outer multiple breakup mode, the inner multiple and outer synchronized breakup mode, the inner and outer synchronized breakup mode, the inner synchronized and outer irregular breakup mode, and the intermittent jet mode, respectively. The dashed box contains the droplets generated in one period of $1/f$. (*b*) Phase diagram of the response modes as the values of f and A vary. The dashed and dash-dotted lines denote the boundaries of different modes roughly.

random again, leading to the I mode. The breakup characteristics are similar to those of an unexcited jet. Figure 9(*b*) also shows the variation tendency of droplet diameter D_o with f. In the frequency range of the S mode, the generation of compound droplets is totally synchronized with actuation; thus, the conservation law of flow rate can be obtained as $(Q_1 + Q_2) = 4/3\pi(D_o/2)^3(1/f)$. Therefore, the size of uniform droplets is related to the perturbation frequency f and the dimensionless average flow rate of core and shell liquids, as given by $f = (Q_1 + Q_2)/(\pi D_o^3/6)$. This suggests the scaling law of $D_o \sim f^{-1/3}$, which is confirmed by the numerical results in figure 9(*b*).

In order to better illustrate the dynamic characteristics of coaxial jet breakup, figure 10 presents the temporal evolution of the position of the outer jet interface tip (sketched in figure 9*b*). As the interface breaks up into droplets, the tip position goes through a sudden jump, and the new tip position indicates the jet breakup length. For the I mode at $f = 0$ and 50, as shown in figure 10(*a*,*d*), the pinch-off positions of the interface are random and the jet breakup length varies within a certain range. At the M mode at $f = 6$ (see figure 10*b*), multiple pinch-off positions exist in one working period of $1/f$. In the S mode at $f = 35$, as demonstrated in figure 10(*c*), the pinch-off positions remain the same, and the jet breakup is periodic.

Figure 11(*a*) demonstrates the effect of actuation frequency f on the breakup of a weak-coupled jet ($r_Q = 0.1$) under constant perturbation amplitude $A = 0.1$. The corresponding diameters of compound droplets D_o and core droplets D_i are presented in figure 11(*b*), respectively. When the coaxial jet is unexcited at $f = 0$, the inner jet experiences a much higher breakup frequency than the outer jet, resulting in the formation of multi-core compound droplets. Numerical results indicate that the natural breakup frequencies of the inner and outer jets are $f_{ni} = 50.2$ and $f_{no} = 17.5$ and the average diameters of the core and compound droplets are approximately 0.143 and 0.43, respectively. When the perturbation frequency is low ($f = 8$), the breakup of the coaxial
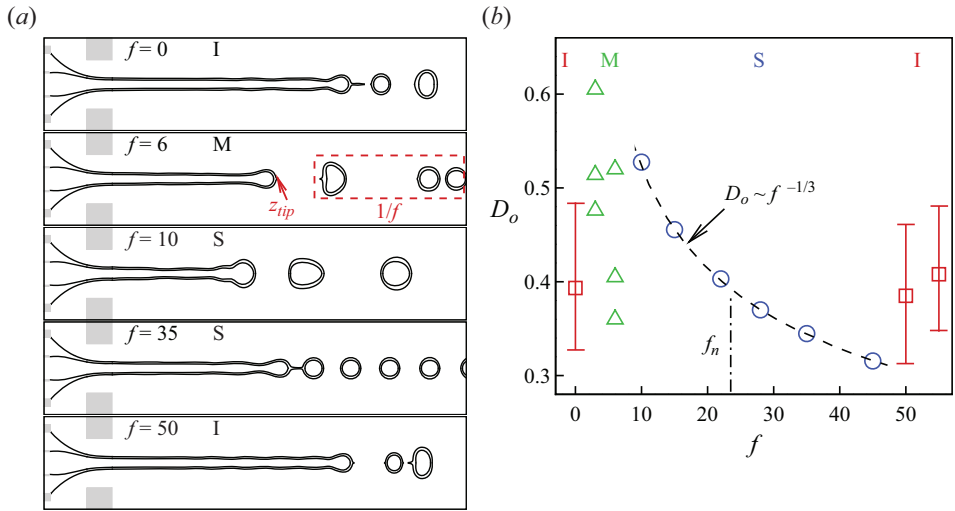
977 A14-15

Figure 9. (a) Interface profiles of the coaxial jet as the perturbation frequency f varies at $A = 0.1$ and $r_Q = 0.5$. (b) Diameters of compound droplets (D_o) under different f, where f_n denotes the natural breakup frequency.
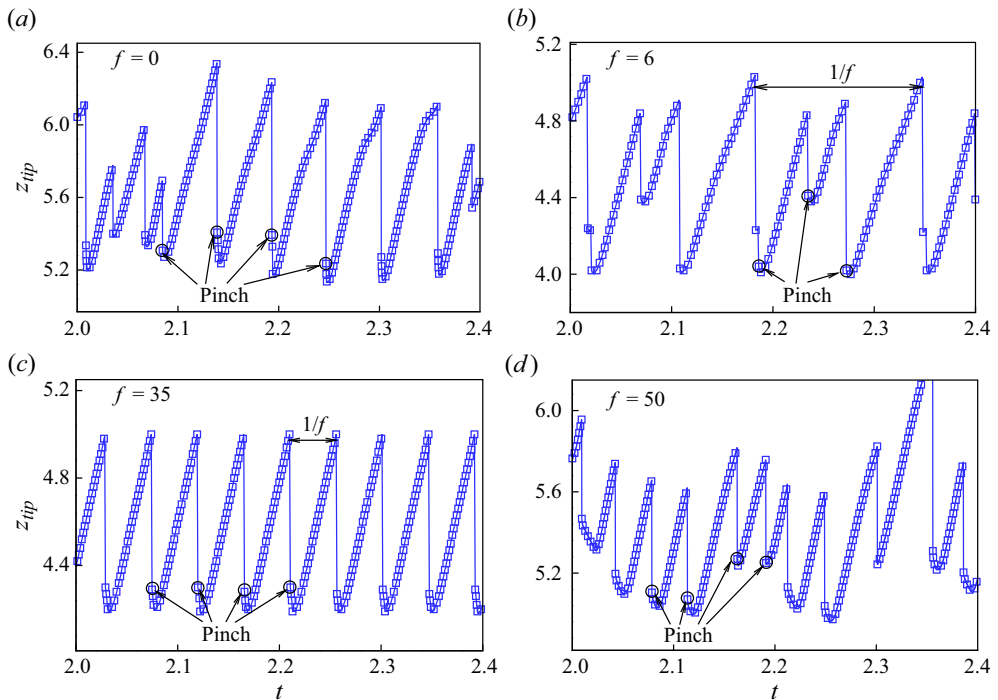

Figure 10. Temporal evolution of the outer jet tip position at (a) $f = 0$, (b) $f = 6$, (c) $f = 35$ and (d) $f = 50$, respectively. The pinch-off positions are also indicated.

jet presents the M-M mode, where both the inner and outer jets form multiple droplets with different sizes during one working period of $1/f$ (see figure 11b). As f gradually increases ($f = 15$), the outer jet enters the S mode first, while the inner jet maintains the M mode (i.e. M-S mode). This occurs because the natural frequency of the outer jet is much lower
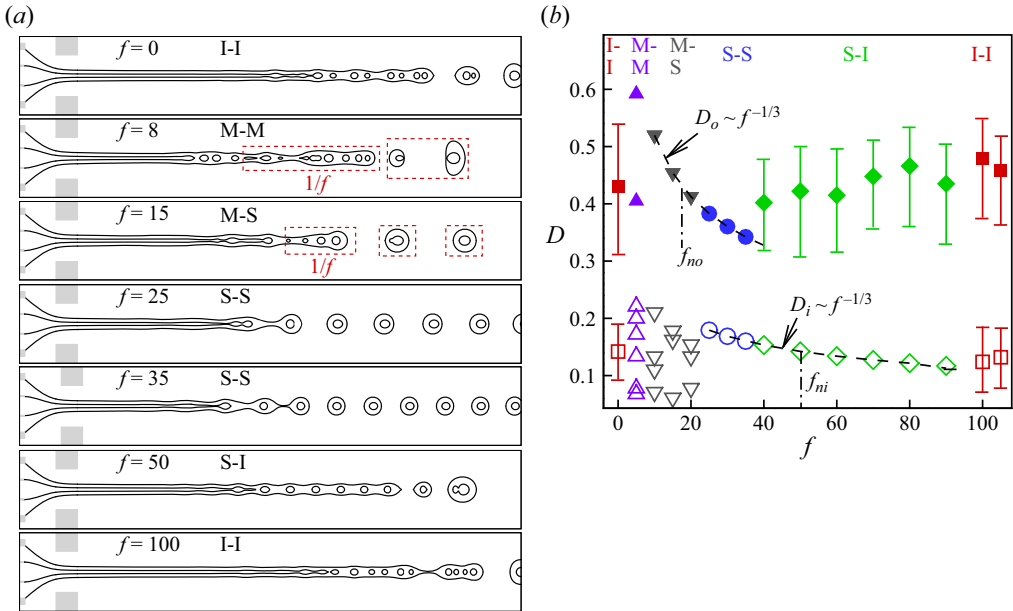
977 A14-16

Figure 11. (*a*) Interface profiles of the coaxial jet as the perturbation frequency f varies at $A = 0.1$ and $r_Q = 0.1$. (*b*) Diameters of inner droplets (D_i, hollow symbols) and compound droplets (D_o, filled symbols) under different f, where f_{ni} and f_{no} denote the natural breakup frequencies of the inner and outer jet, respectively.

than that of the inner jet. When the frequency increases to $f = 25$, both the inner and outer jets break at the S mode with single-core droplet formation. In this S-S mode, the size of compound droplets can be adjusted by the actuation frequency. As f increases further ($f = 50$), the jet breakup transitions to the S-I mode. In this mode, the breakup of the outer jet loses its periodicity and returns to the I mode again, where the droplet size is located within some ranges. However, the size of the inner droplets remains uniform. At very high frequency ($f = 100$), both the inner and outer jets break at the I mode (i.e. I-I), which is similar to the unexcited jet. Notably, in the synchronized region of the inner and outer jets, the droplet size follows the relationship $D_o \sim f^{1/3}$ and $D_i \sim f^{1/3}$, respectively, as shown clearly in figure 11(*b*).

Figure 12 presents the temporal evolution of the interface tip positions of both the inner and outer jets. The results show that the pinch-off positions and the periodicity of the jet breakup are significantly affected by the actuation frequency f. For the I-I mode at $f = 0$ and 100, as shown in figure 12(*a*,*f*), the pinch-off positions of the inner and outer interfaces are rather random, suggesting that the jet breakup length varies with time and there is no periodicity for jet breakup. For the M-M mode at $f = 8$ (see figure 12*b*), multiple pinch-off positions exist for both the inner and outer jets in one working period of $1/f$. For the M-S mode at $f = 15$, the outer jet has a constant pinch-off position while multiple pinch-off positions exist for the inner jet, as shown in figure 12(*c*). In the S-S mode at $f = 35$, both the inner and outer jets have constant pinch-off positions, and the interface evolution is periodic (see figure 12*d*). In the S-I mode at $f = 50$, the inner jet has a constant pinch-off position while random pinch-off positions exist for the outer jet, as shown in figure 12(*e*).
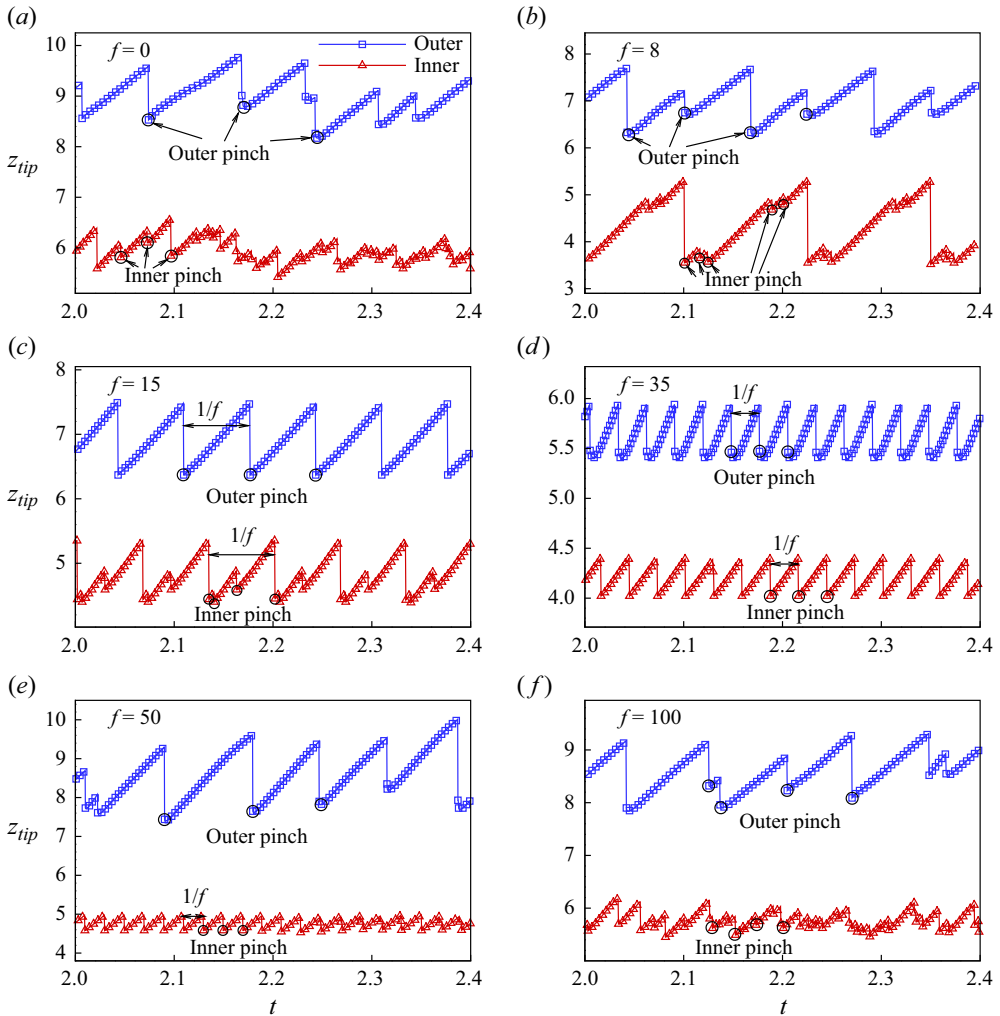
Figure 12. Temporal evolution of inner and outer jet tip positions at $(a) f = 0$, $(b) f = 8$, $(c) f = 15$, $(d) f = 35$, $(e) f = 50$ and $(f) f = 100$, respectively. The pinch-off positions are also indicated.

4.3. *Effect of actuation amplitude*

We also investigate the effect of actuation amplitude A on the breakup of the coaxial liquid jet. An increase of A can enhance the initial perturbations on the coaxial liquid cone and the jet downstream. As illustrated in figures 7(b) and 8(b), the variation of A can lead to the transition between different response modes, and the jet even becomes unstable at a high value of A and low value of f. In this section we focus on the effect of A under moderate values of f, where the coaxial cone-jet structure can be maintained consistently.

Figure 13(a) shows the breakup profiles of the coaxial jet at $r_Q = 0.5$, under a fixed $f = 40$ with A varying. When A is at relatively low value (e.g. $A = 0.03$), the external perturbation is too weak to influence the jet breakup, and the coaxial jet exhibits a non-uniform size distribution of droplets in the I mode. At moderate values of A, as the perturbation frequency f falls within the synchronized breakup range, the coaxial jet can exhibit the S mode, displaying periodic behaviour and a consistent breakup length with no
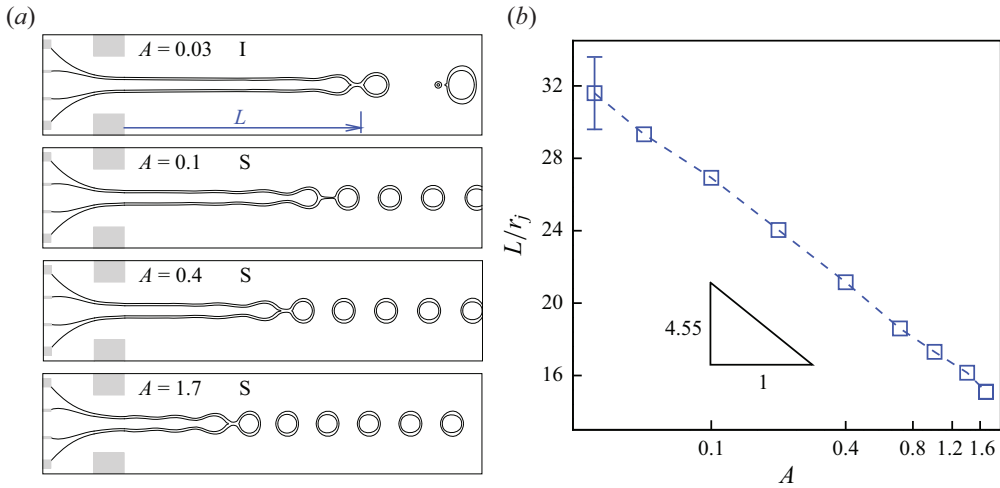
Figure 13. (*a*) Interface profiles and (*b*) breakup length of the coaxial jet under different A at $f = 40$ and $r_Q = 0.5$. The triangle denotes the theoretical variation slope of -4.55 that is predicted in § 5.3.

variation on droplet size. However, the variation of A can significantly affect the breakup length of the jet. The relationship between jet breakup length L and perturbation amplitude A is given in figure 13(*b*), in which L is measured as the distance between the pinch-off position to the orifice exit (see the sketch in figure 13*a*) and rescaled by the radius r_j of the coaxial jet. This operation is for the convenience of comparing the numerical results with linear instability analysis, in which r_j is chosen as the characteristic length. It is notable that the jet breakup length falls within certain ranges with its average value in the I mode, whereas it remains constant in the S mode. The jet breakup length appears to follow the law $L \sim -\ln A$, and we provide theoretical analysis on the jet breakup length in § 5.3.

Figure 14(*a*) shows the breakup profiles of the coaxial jet at $r_Q = 0.1$, under a varying A for a fixed $f = 15$. Similarly, when A is relatively small (e.g. $A = 0.03$), the external perturbation is too weak to have any significant effect on the coaxial jet breakup, and the jet presents the I-I mode. However, as A gradually increases, the external perturbation can affect the coaxial jet breakup significantly. Specifically, the coaxial jet breakup exhibits the M-S mode for $A = 0.1$ and 0.4, while the mode changes to the S-S mode as $A = 1$. The breakup lengths of the inner and outer jets (denoted by L_i and L_o, respectively) are defined as the distance between the pinch-off positions of the inner and outer jet to the orifice exit (see figure 14*a*), respectively, and the jet breakup lengths rescaled by r_j are shown in figure 14(*b*). In the I-I mode, the values of L_i and L_o locate within a certain range due to the non-periodic breakup characteristics. Therefore, both the average length and the error bars are presented simultaneously. In the M-S mode the value of L_i falls within a certain range while that of L_o remains constant. In the S-S mode, both the inner and outer jet breakup lengths maintain the same value. Our analysis indicates that the relationship $L_i \sim -\ln A$ is a suitable model for the inner jet, whereas this model does not apply to the outer jet. Theoretical analysis on the jet breakup length will be given in § 5.3.

4.4. *Effect of liquid flow rates*

The diameter and velocity of a coaxial liquid jet can be significantly affected by the flow rates of the core, shell and focusing liquids. Therefore, the liquid flow rates are
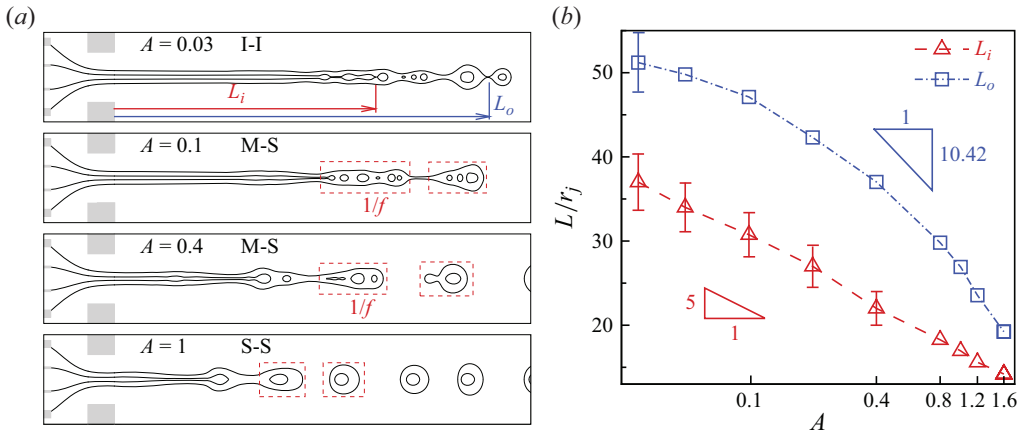
Figure 14. (*a*) Interface profiles and (*b*) breakup length of the coaxial jet under different A at $f = 15$ and $r_Q = 0.1$. The triangles denote the theoretical variation slope of the inner and outer jet (-5 and -10.42, respectively) that are predicted in § 5.3.

supposed to affect the natural frequency and the synchronized region of the coaxial liquid jet. According to the definition of the dimensionless parameter in numerical simulations, $Re \sim U_3 \sim Q_3$, $r_{Q1} = Q_1/Q_3$ and $r_{Q2} = Q_2/Q_3$. Therefore, the change of focusing flow rate Q_3 corresponds to the variation of Re under a constant value of $Re \cdot (r_{Q1} + r_{Q2})$, and the change of coaxial jet flow rates $Q_1 + Q_2$ corresponds to the variation of $r_{Q1} + r_{Q2}$ under a constant value Re, respectively. Figure 15(*a*) shows the effect of focusing flow rate (non-dimensionalized by Re) for a strong-coupled jet at $r_Q = 0.5$ and a constant perturbation amplitude of $A = 0.1$, where f_n, f_c and f_l are the natural frequency, upper critical frequency and lower critical frequency of the synchronized region, respectively. It is worth noting that f_n falls within a certain range due to the random breakup of the undisturbed jet, and its average value is given along with the error bars. As for the critical frequencies f_c and f_l, error bars also exist due to the uncertainty on the determination of mode boundaries. It is clear that f_n, f_c and f_l all increase with Re increasing, indicating that increasing the focusing flow rate can increase both the natural frequency and critical frequencies of the synchronized region. Figure 15(*b*) shows the effect of the sum flow rate of the inner and outer jet (non-dimensionalized by $r_{Q1} + r_{Q2}$) at $r_Q = 0.5$ and $A = 0.1$, which demonstrates that f_n, f_c and f_l all decrease as $r_{Q1} + r_{Q2}$ gradually increases. This finding suggests that increasing the coaxial jet flow rates can decrease both the natural frequency and critical frequencies of the synchronized region.

The breakup behaviours of the weak-coupled jet are more complex due to the independent breakup of the inner and outer jets. Figure 15(*c,d*) shows that the natural frequency of the inner jet (f_{ni}) is significantly greater than that of the outer jet (f_{no}). In addition, the upper and lower critical frequencies of the inner jet (f_{ci} and f_{li}, respectively) are also much larger than those of the outer jet (f_{co} and f_{lo}, respectively). It is also observed that the synchronized frequency range of the inner jet is much wider than that of the outer jet. Similar to the situation of the strong-coupled jet, an increase of Re or a decrease of $r_{Q1} + r_{Q2}$ can lead to the increase of natural frequency and critical frequency of both the inner and outer jets, as shown in figure 15(*c,d*), respectively. In § 5 we further provide theoretical predictions for the natural breakup frequency and the upper critical frequency based on the instability analysis of simplified single jet models for coaxial jets under strong and weak coupling conditions.
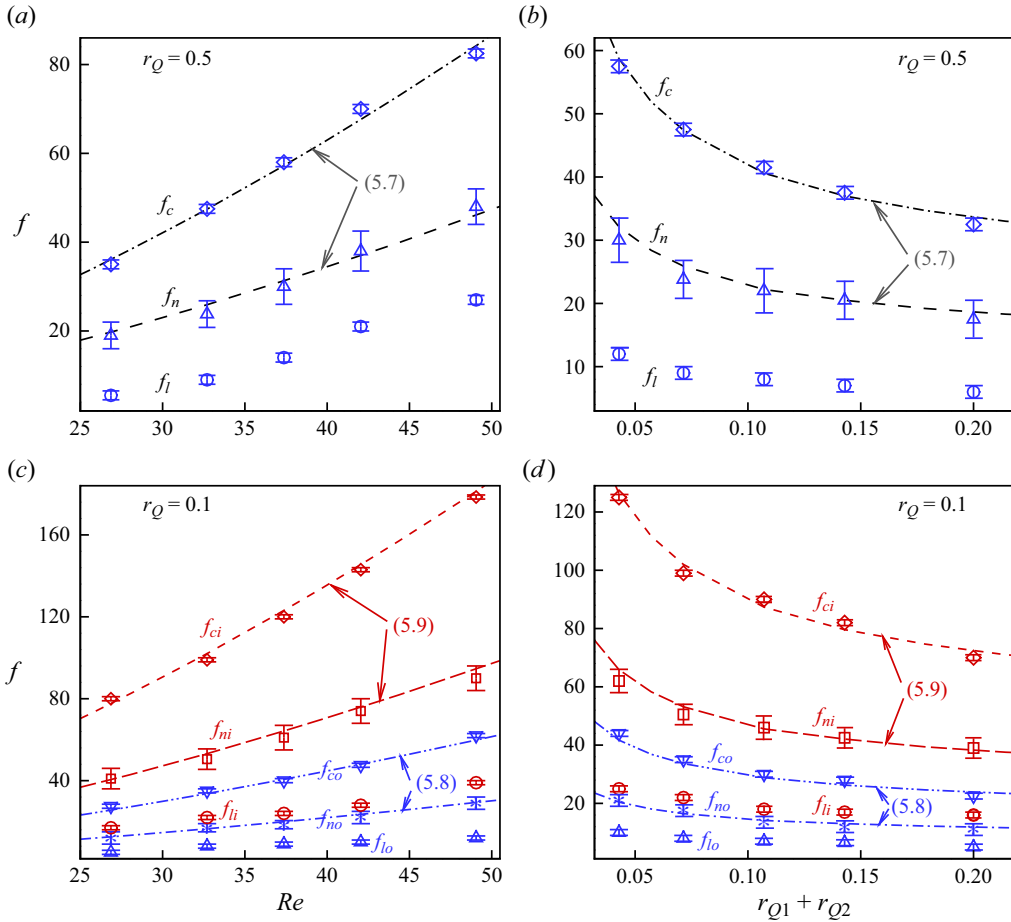
977 A14-20

Figure 15. The natural frequency (f_n), lower critical frequency (f_l) and upper critical frequency (f_c) for a strong-coupled coaxial jet at $r_Q = 0.5$ under constant perturbation amplitude of $A = 0.1$ as the values of (*a*) Re varies at fixed $Re \cdot (r_{Q1} + r_{Q2}) = 2.336$ and (*b*) $r_{Q1} + r_{Q2}$ varies at fixed $Re = 32.7$. The natural frequency (f_{no}), lower critical frequency (f_{lo}) and upper critical frequency (f_{co}) of the outer jet and those of the inner jet (denoted by f_{ni}, f_{li} and f_{ci}, respectively) for a weak-coupled coaxial jet at $r_Q = 0.1$ under constant perturbation amplitude of $A = 0.1$ as the values of (*c*) Re varies at fixed $Re \cdot (r_{Q1} + r_{Q2}) = 2.336$ and (*d*) $r_{Q1} + r_{Q2}$ varies at fixed $Re = 32.7$. The symbols denote the numerical results and the lines denote the theoretical predictions of scaling analysis in § 5.2.

The effect of relative flow rate between the inner and outer jets on coaxial jet breakup is also investigated. Figure 16(*a*) shows the breakup profiles of the coaxial liquid jet as r_Q varies under constant values of $f = 30$ and $A = 0.1$, where the liquid flow rates are constant at $Re = 32.7$ and $r_{Q1} + r_{Q2} = 0.0714$. It is observed that in a wide range of r_Q ($r_Q = 0.1$, 0.35 and 0.6), the inner and outer jets breakup synchronously with external perturbations under the S-S mode, resulting in uniform compound droplets with a single core inside. By varying r_Q, the relative size between the core and shell droplets can be well controlled, which has practical significance in real applications. However, at a very low value of r_Q ($r_Q = 0.05$), the inner jet loses its periodicity and the breakup of the coaxial jet presents the M-S mode, showing that the generation of core droplets cannot be controlled precisely. The reason for the aperiodicity on inner droplet formation can
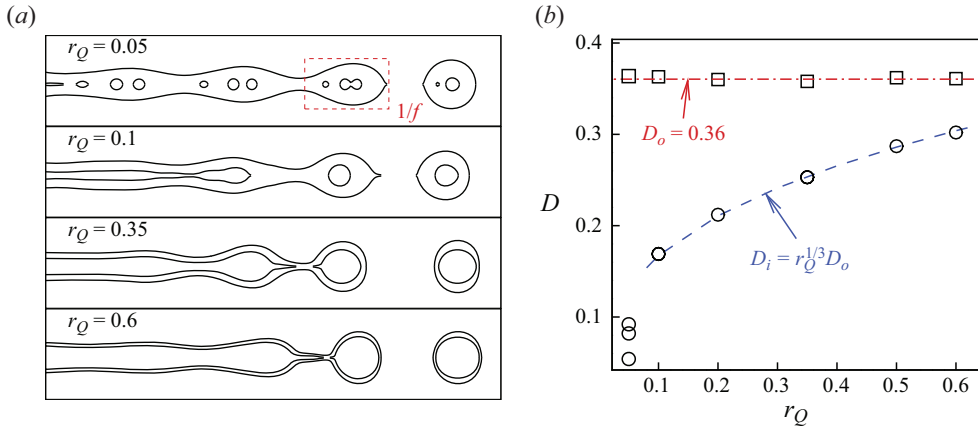
Figure 16. (*a*) Profiles of a coaxial jet at different r_Q under constant values of $f = 30$ and $A = 0.1$. (*b*) Diameters of inner and outer droplets as r_Q changes.

be explained qualitatively as: the inner jet diameter is very small at a low value of r_Q; therefore, the natural frequency and the frequency range of the synchronized region differs significantly between the inner and outer jets. As the value of r_Q gradually decreases, the natural frequency of the inner jet (f_{ni}) increases, and the lower critical frequency of the inner jet (f_{li}) increases correspondingly. As f_{li} becomes larger than the upper critical frequency of the outer jet (f_{co}), the frequency range for the S-S mode vanishes, thus, the inner jet presents the M mode while the outer jet maintains the S mode. Figure 16(*b*) presents the diameters of both the inner and outer droplets as r_Q varies, showing that the outer droplets diameter D_o keeps almost unchanged while the inner droplet diameter D_i decreases with the decrease of r_Q. Specifically, inner droplets with multiple diameters are formed at the M-S mode when $r_Q = 0.05$. In the synchronized region the outer and inner droplet diameters can be predicted theoretically by the dimensionless flow rates and frequency, i.e. $D_o = (6(Q_1 + Q_2)/\pi f)^{1/3}$ and $D_i = r_Q^{1/3} D_o$, respectively. Therefore, the outer droplet diameter D_o keeps unchanged at fixed f, which is calculated as $D_o = 0.36$ for the cases considered in figure 16(*a*). The theoretical prediction agrees well with the numerical results.

5. Theoretical analysis

5.1. *Linear instability*

In order to give the theoretical analysis on the breakup characteristics of coaxial liquid jets, we carry out a temporal instability analysis considering the perturbation growth on the jet interface. We mainly focus on the locally convective instability of the liquid jets, where the perturbation only propagates downstream the jet that induces the generation of droplets (Lin 2003; Eggers & Villermaux 2008). Such an assumption is appropriate for the coaxial liquid jets with parallel flow characteristics downstream of the orifice. For convenience, we can simplify the coaxial jet to a single jet model at different interface coupling situations, as illustrated in figure 17. On one hand, at relatively large r_Q that corresponds to the jet diameter ratio $\kappa \to 1$, the coupling of interfaces is strong and the coaxial jet can be simplified as a single liquid jet where the shell phase is neglected, and the equivalent interfacial tension equals the sum of the inner and outer jets, as shown in
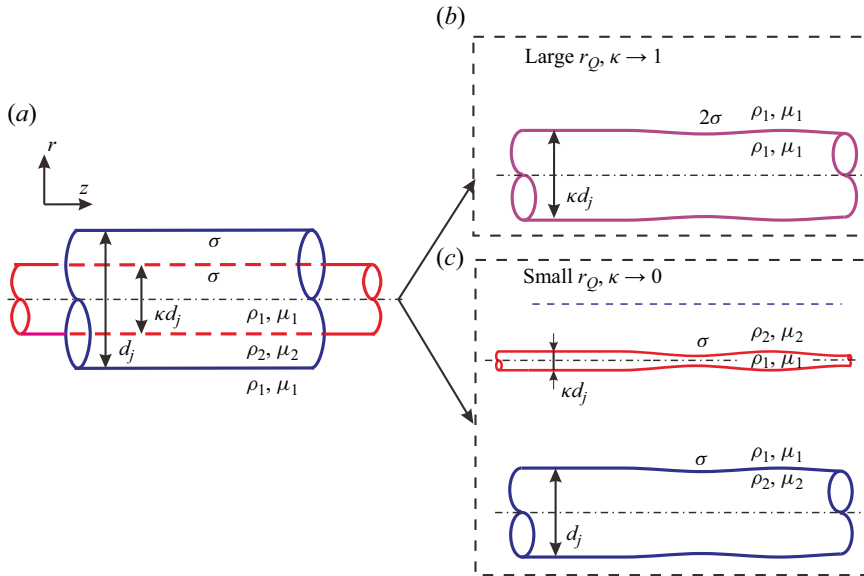
Figure 17. (*a*) Theoretical model for the coaxial liquid jet, where the diameter ratio between the inner and outer jet is denoted by κ. (*b*) Simplified single jet model as $\kappa \to 1$, corresponding to the situation of large r_Q. (*c*) Simplified single jet model as $\kappa \to 0$, corresponding to the situation of small r_Q.

figure 17(*b*). Therefore, the diameter and the surface tension coefficient of the simplified jet is κd_j and 2σ, respectively, where d_j is the diameter of the coaxial jet. On the other hand, at relatively low r_Q ($\kappa \to 0$), the coupling effect between the double interfaces is very weak, thus, the coaxial jet can be decoupled as two single jets, as illustrated in figure 17(*c*). The diameters of the inner and outer jets are κd_j and d_j, respectively. In our theoretical model we assume equal velocities of the inner jet, the outer jet and the surrounding flow, which has been proved reasonable for the all-liquid system in previous studies (Gañán-Calvo & Riesco-Chueca 2006; Gañán-Calvo *et al.* 2007). The simplified single jet models for weak- and strong-coupled coaxial jets enable us to study behaviours of coaxial jet breakup at extreme conditions.

For the linear instability analysis, we choose the jet radius $d_j/2$ and the average velocity U_j as the characteristic length and velocity, respectively. The dimensionless parameters for the single jet models in theoretical analysis are the Weber number $We_t = \rho_j U_j^2 d_j/2\sigma$, the Reynolds number $Re_t = \rho_j U_j d_j/2\mu_j$, the density ratio $S = \rho_e/\rho_j$ and the viscosity ratio $N = \mu_e/\mu_j$, where ρ_j and μ_j are the density and viscosity of the liquid jet while ρ_e and μ_e are those of the surrounding environment, respectively. The theoretical model is solved through the normal mode method, in which the terms such as flow velocity, pressure and interface position in Navier–Stokes equations are decomposed to basic quantities and small axisymmetric perturbations with the Fourier form $\sim e^{i(kz-\omega t)}$. It is notable that k is the dimensionless wavenumber, $\omega = \omega_r + i\omega_i$ is the dimensionless complex frequency, where ω_i and $-\omega_r$ denote the growth rate and temporal frequency of perturbations, respectively. The perturbations with $\omega_i > 0$ are temporally unstable while those with $\omega_i < 0$ are stable invariably. In our work, the perturbation frequency $-\omega_r$ will be utilized to predict the natural and critical frequencies of coaxial jet breakup under different coupling situations (see § 5.2), and the growth rate ω_i will be used to analyse the jet breakup length, as shown in § 5.3. The governing equations and boundary conditions for the single jet model are

977 A14-23

similar to those in Si *et al.* (2009) and are simply shown in Appendix A. Specifically, for the model at $\kappa \to 1$ shown in figure 17(*b*), we have $\rho_j = \rho_e = \rho_1$ and $\mu_j = \mu_e = \mu_1$. For the models at $\kappa \to 0$ shown in figure 17(*c*), the inner jet model corresponds to $\rho_j = \rho_1$, $\rho_e = \rho_2$, $\mu_j = \mu_1$ and $\mu_e = \mu_2$, while the outer jet model corresponds to $\rho_j = \rho_2$, $\rho_e = \rho_1$, $\mu_j = \mu_2$ and $\mu_e = \mu_1$.

5.2. *Prediction of natural and critical frequencies*

Based on the results obtained from the linear instability analysis, we can give the scaling analysis on the natural frequency and the upper critical frequency of the synchronized breakup region. For a single liquid jet with average velocity U_j and diameter d_j, the natural breakup frequency f_n is directly related to the jet oscillation frequency $-\omega_{rm}$ that corresponds to the maximum growth rate of the perturbation wave (whose wavenumber is denoted as k_m), with the quantitative estimation of

$$f_n = \frac{-\omega_{rm}U_j}{\pi d_j}. \tag{5.1}$$

In the flow focusing process, d_j and U_j can be estimated by the simple scaling law of $d_j = d \cdot [Q_j/(Q_j + Q_e)]^{1/2}$ and $U_j = 4Q_j/\pi d_j^2$, respectively. Here, Q_j and Q_e denote the flow rates of the liquid jet and co-flowing liquid and d is the orifice diameter. Therefore, the natural frequency can be expressed as

$$f_n = \frac{4}{\pi^2 d^3} \cdot \frac{(-\omega_{rm})(Q_j + Q_e)^{3/2}}{Q_j^{1/2}}. \tag{5.2}$$

Similarly, the upper critical frequency below which the external perturbation can modulate the jet breakup can be expressed as

$$f_c = \frac{4}{\pi^2 d^3} \cdot \frac{(-\omega_{rc})(Q_j + Q_e)^{3/2}}{Q_j^{1/2}}, \tag{5.3}$$

where $-\omega_{rc}$ is critical frequency that corresponds to the cutoff wavenumber (k_c) of the perturbation growth rate. When the wavenumber is larger than k_c, the perturbation growth rate becomes smaller than zero, and the liquid jet is invariably stable.

In this study, as we have simplified the coaxial jet to single jet models under different coupling situations, the natural and upper critical frequencies can be predicted similarly. For a strong-coupled jet, the coaxial liquid can be reduced to the single jet model in figure 17(*b*), and the natural and upper critical frequencies are expressed as

$$\left.\begin{aligned} f_n &= \frac{4}{\pi^2 d^3} \cdot \frac{(-\omega'_{rm})(Q_1 + Q_2 + Q_3)^{3/2}}{(Q_1 + Q_2)^{1/2}}, \\ f_c &= \frac{4}{\pi^2 d^3} \cdot \frac{(-\omega'_{rc})(Q_1 + Q_2 + Q_3)^{3/2}}{(Q_1 + Q_2)^{1/2}}, \end{aligned}\right\} \tag{5.4}$$

where $-\omega'_{rm}$ is the frequency of the perturbation wave with the maximum growth rate, and $-\omega'_{rc}$ is the frequency that corresponds to the cutoff wavenumber, as sketched in figure 18(*a,b*).
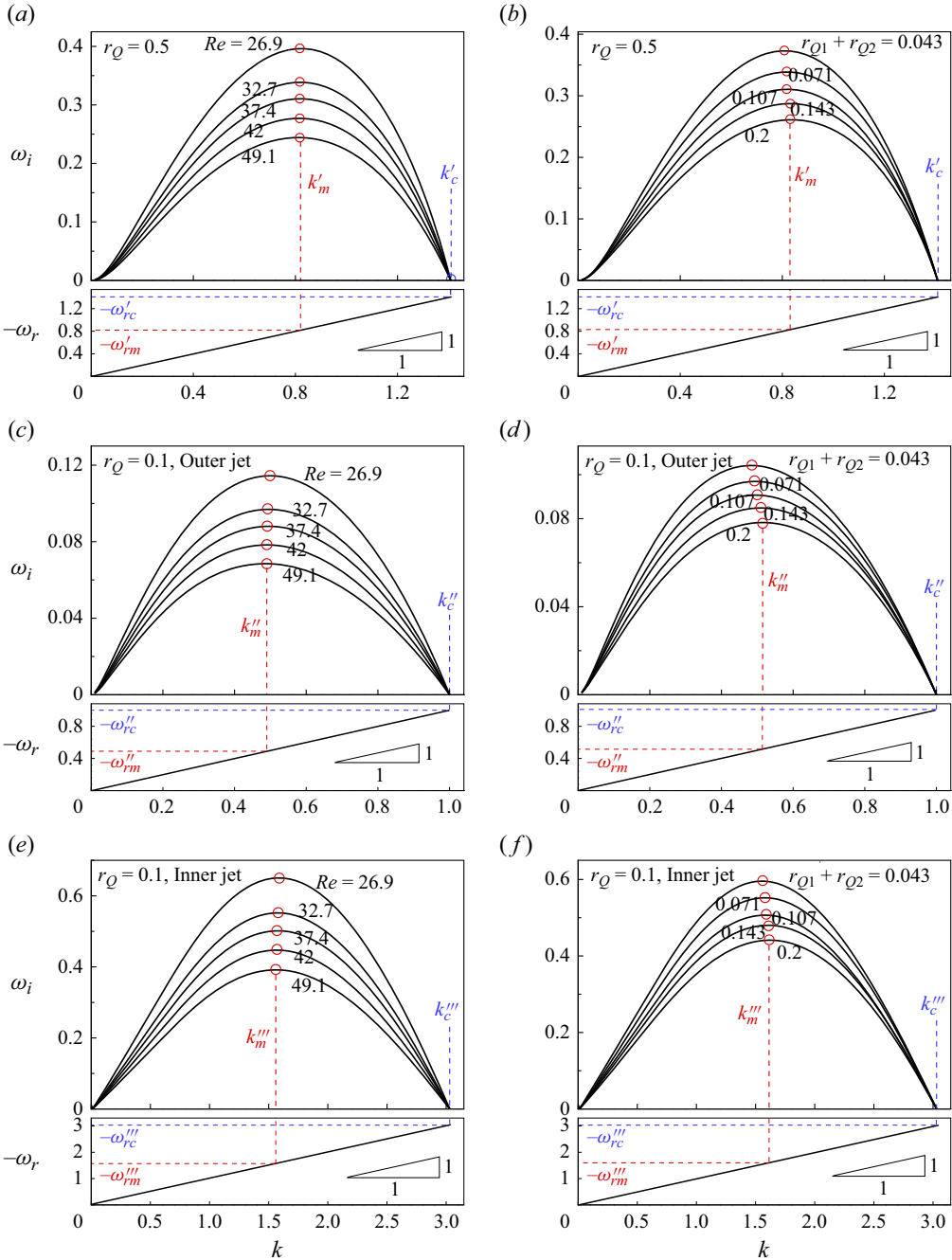
977 A14-24

Figure 18. Perturbation growth rate ω_i and frequency $-\omega_r$ versus wavenumber k for different single jet models given in figure 17. (*a*) Variation of *Re* under fixed $Re \cdot (r_{Q1} + r_{Q2})$ for the strong-coupled jet at $r_Q = 0.5$, corresponding to $\kappa = 0.71$. (*b*) Variation of $r_{Q1} + r_{Q2}$ under fixed *Re* for the strong-coupled jet at $r_Q = 0.5$. (*c*) Variation of *Re* under fixed $Re \cdot (r_{Q1} + r_{Q2})$ for the outer jet of the weak-coupled jet at $r_Q = 0.1$, corresponding to $\kappa = 0.33$. (*d*) Variation of $r_{Q1} + r_{Q2}$ under fixed *Re* for the outer jet of the weak-coupled jet at $r_Q = 0.1$. (*e*) Variation of *Re* under fixed $Re \cdot (r_{Q1} + r_{Q2})$ for the inner jet of the weak-coupled jet at $r_Q = 0.1$. (*f*) Variation of $r_{Q1} + r_{Q2}$ under fixed *Re* for the inner jet of the weak-coupled jet at $r_Q = 0.1$.

As for a weak-coupled coaxial liquid jet that can be viewed as two single jets, as shown in figure 17(*c*), the natural and upper critical frequencies of the outer jet and inner jet can be expressed as

$$
\left.\begin{aligned}
f_{no} &= \frac{4}{\pi^2 d^3} \cdot \frac{(-\omega''_{rm})(Q_1 + Q_2 + Q_3)^{3/2}}{(Q_1 + Q_2)^{1/2}}, \\
f_{co} &= \frac{4}{\pi^2 d^3} \cdot \frac{(-\omega''_{rc})(Q_1 + Q_2 + Q_3)^{3/2}}{(Q_1 + Q_2)^{1/2}},
\end{aligned}\right\}
\tag{5.5}
$$

$$
\left.\begin{aligned}
f_{ni} &= \frac{4}{\pi^2 d^3} \cdot \frac{(-\omega'''_{rm})(Q_1 + Q_2 + Q_3)^{3/2}}{(Q_1 + Q_2)^{1/2}}, \\
f_{ci} &= \frac{4}{\pi^2 d^3} \cdot \frac{(-\omega'''_{rc})(Q_1 + Q_2 + Q_3)^{3/2}}{(Q_1 + Q_2)^{1/2}},
\end{aligned}\right\}
\tag{5.6}
$$

where $-\omega''_{rm}$ and $-\omega''_{rc}$ are the oscillation frequencies that correspond to the perturbation wave with the maximum growth rate and the cutoff wavenumber of the outer jet model (see figure 18*c*,*d*), while $-\omega'''_{rm}$ and $-\omega'''_{rc}$ are the oscillation frequencies of the perturbation waves with the maximum growth rate and the cutoff wavenumber of the inner jet model, respectively (see figure 18*e*,*f*).

According to our definition of parameters, the dimensionless frequency can be written in the form of Re, r_{Q1} and r_{Q2}, i.e.

$$
f_n = C \cdot \frac{(-\omega'_{rm})(r_{Q1} + r_{Q2} + 1)^{3/2}}{(r_{Q1} + r_{Q2})^{1/2}}, \quad f_c = C \cdot \frac{(-\omega'_{rc})(r_{Q1} + r_{Q2} + 1)^{3/2}}{(r_{Q1} + r_{Q2})^{1/2}}, \tag{5.7a,b}
$$

for the strong-coupled jet, and

$$
f_{no} = C \cdot \frac{(-\omega''_{rm})(r_{Q1} + r_{Q2} + 1)^{3/2}}{(r_{Q1} + r_{Q2})^{1/2}}, \quad f_{co} = C \cdot \frac{(-\omega''_{rc})(r_{Q1} + r_{Q2} + 1)^{3/2}}{(r_{Q1} + r_{Q2})^{1/2}}, \tag{5.8a,b}
$$

$$
f_{ni} = C \cdot \frac{(-\omega'''_{rm})(r_{Q1} + r_{Q2} + 1)^{3/2}}{(r_{Q1} + r_{Q2})^{1/2}}, \quad f_{ci} = C \cdot \frac{(-\omega'''_{rc})(r_{Q1} + r_{Q2} + 1)^{3/2}}{(r_{Q1} + r_{Q2})^{1/2}}, \tag{5.9a,b}
$$

for the outer and inner jet of the weak-coupled jet, respectively. In these equations, C is a constant with its value decided by the geometrical parameters D_2 and d, which equals a specific value of 8.5 in our simulations.

It is notable that (5.7), (5.8) and (5.9) do not contain Re explicitly. However, the variation of Re in figure 15(*a*,*c*) also leads to the corresponding change of $r_{Q1} + r_{Q2}$, indicating that the single variation of focusing flow rate can change the natural breakup frequency and upper critical frequency of the synchronized region.

The oscillation frequencies that correspond to the maximum perturbation growth rate and the cutoff wavenumber in (5.7), (5.8) and (5.9) can be determined by linear instability analysis on the simplified single jet models. Figure 18(*a*,*b*) shows the perturbation growth rate curves and the oscillation frequency curves of the simplified single jet for the strong-coupled jet at $r_Q = 0.5$ (corresponding to $\kappa = 0.71$), considering (*a*) the variation of Re under fixed $Re \cdot (r_{Q1} + r_{Q2})$ and (*b*) the variation of $r_{Q1} + r_{Q2}$ under fixed Re, respectively. It is notable that the variation of Re or $r_{Q1} + r_{Q2}$ affects the growth rate curves significantly but hardly changes the oscillation frequency curves. For each curve, we can determine the values of the most unstable wavenumber k'_m and the cutoff wavenumber

977 A14-26

k'_c and then obtain the values of $-\omega'_{rm}$ and $-\omega'_{rc}$, respectively. It is notable that for the cases considered here, the value of the dimensionless frequency is equal to that of the wavenumber invariably (i.e. $-\omega'_{rm} = k'_m$ and $-\omega'_{rc} = k'_c$), indicating that the perturbation propagates with a dimensionless phase velocity of $-\omega'_r/k = 1$. Therefore, if one stands on the axial local framework along with the liquid jet, the interface disturbance only grows temporally and hardly propagates upstream or downstream of the jet, which is similar to the standard temporal stability analysis of the capillary jet (Lin 2003; Eggers & Villermaux 2008). The results indicate that the variation of Re or $r_{Q1} + r_{Q2}$ mainly affects the perturbation growth rate ω_i but only has a tiny effect on the wavenumber corresponding to the maximum growth rate and the cutoff wavenumber. In all cases examined in figure 18(a,b), k'_c is at a constant value of 1.41 and k'_m only varies slightly within 0.82 ± 0.01. As for the weak-coupled jet at $r_Q = 0.1$ (corresponding to $\kappa = 0.33$), the outer and inner jets are analysed independently. For the outer jet, the perturbation growth rate curves and the oscillation frequency curves as Re varies under fixed $Re \cdot (r_{Q1} + r_{Q2})$ and those as $r_{Q1} + r_{Q2}$ varies under fixed Re are given in figure 18(c,d), respectively. Similarly, the variation of Re or $r_{Q1} + r_{Q2}$ only has a tiny effect on the wavenumber corresponding to the maximum growth rate and the cutoff wavenumber. Within the parameter range we consider, $-\omega''_{rm} = k''_m$ and $-\omega''_{rc} = k''_c$, with $k''_c = 1$ and $k''_m = 0.49 \pm 0.01$. For the inner jet, the perturbation growth rate curves and the oscillation frequency curves as Re varies under fixed $Re \cdot (r_{Q1} + r_{Q2})$ and those as $r_{Q1} + r_{Q2}$ varies under fixed Re are given in figure 18(e,f), respectively. Similarly, the cutoff wavenumber and the wavenumber corresponding to the maximum growth rate hardly change, in which $-\omega'''_{rm} = k'''_m = 1.58 \pm 0.01$ and $-\omega'''_{rc} = k'''_c = 3$. With the wavenumber being determined, the theoretical predictions of f_n and f_c for the strong-coupled jet and f_{no}, f_{co}, f_{ni} and f_{ci} for the weak-coupled jet can be obtained according to (5.7)–(5.9). The theoretical results are depicted as lines in figure 15, showing a good agreement with the numerical results.

5.3. *Predictions of jet breakup length*

For a liquid jet with radius r_j, the perturbation on the interface develops with growth rate ω_i and initial magnitude η_0. Under the linear instability frame, they follow the relationship

$$r_j = \eta_0\, e^{\omega_i t_b}, \tag{5.10}$$

where t_b is the jet breakup time, and it can be expressed as

$$t_b = \frac{1}{\omega_i} \ln \frac{r_j}{\eta_0}. \tag{5.11}$$

The jet breakup length L_j can be calculated through multiplying the jet velocity U_j with t_b, i.e.

$$L_j = \frac{U_j}{\omega_i} \ln \frac{r_j}{\eta_0}. \tag{5.12}$$

Previous research by Moallemi *et al.* (2016) has established that the initial interface perturbation of a single jet is related to the flow rate perturbation A_j of the liquid jet through a linear relationship, i.e. $\eta_0 \sim A_j$. Moreover, the flow rate perturbation A_j has been found to be almost in direct proportion to that of the capillary tube A, i.e. $A_j \sim A$, as shown in figures 3(a) and 5(a), respectively. Therefore, the relationship between L_j and A can be

expressed as

$$L_j \sim \frac{U_j}{\omega_i} \ln \frac{r_j}{A}. \tag{5.13}$$

It is notable that in linear instability analysis, r_j and U_j are chosen as the characteristic length and velocity, respectively. Therefore, (5.13) gives the relationship $L_j \sim -\ln A$, and the slope can be decided by the value of $-1/\omega_i$.

For the coaxial liquid jet, as we have simplified the coaxial jet to a single jet at different coupling situations, the jet breakup length can be predicted similarly. For the strong-coupled jet ($r_Q = 0.5$) in figure 13, the jet breakup length L rescaled by r_j obeys the law of $L/r_j \sim -\ln A$. To estimate the slope of the curve, the growth rate ω_i at the corresponding actuation frequency ($f = 40$) can be obtained from the growth rate curve, which corresponds to the curve $Re = 32.7$ in figure 18(a). The frequency $f = 40$ corresponds to a wavenumber $k = 1.19$ at which the growth rate $\omega_i \approx 0.22$. Therefore, the estimated slope is about -4.55. Figure 13(b) also gives the slope predicted by the theory, as shown by the triangle, which agrees well with the numerical results.

The breakup length of the inner and outer jets for the weak-coupled coaxial jet at $r_Q = 0.1$ can be analysed independently. Based on the simplified single jet models, the breakup length of the inner and outer jets can be expressed as

$$L_i \sim \frac{U_j}{\omega_i} \ln \frac{r_j}{A} \tag{5.14}$$

and

$$L_o \sim \frac{U_j}{\omega_i} \ln \frac{r_j}{A}. \tag{5.15}$$

Choosing r_j and U_j as the characteristic scales, (5.14) and (5.15) are simplified as $L_i \sim -\ln A$ and $L_o \sim -\ln A$. For the numerical results in figure 14, the slopes on the variation of L_i/r_j and L_o/r_j with A are decided by the growth rates of the inner and outer jet, respectively. According to figure 18(c,e), the growth rate ω_i at $f = 15$ can be obtained from the curve that corresponds to the situation $Re = 32.7$. The frequency $f = 15$ corresponds to a wavenumber $k = 0.45$, and the growth rates of the inner and outer jets are $\omega_i \approx 0.2$ and 0.096, respectively. Therefore, the slope $-1/\omega_i$ of the inner and outer jets can be estimated as -5 and -10.42, respectively. Figure 14(b) also gives the theoretical slope for the inner and outer jets, respectively, as shown by the triangles. It is clear that the theoretical prediction of the inner jet agrees well with the numerical results, while that of the outer jet diverges significantly from the numerical results. The results suggest that the breakup of the inner droplet brings in additional perturbation and, thus, has a huge influence on the breakup length of the outer jet, even in the weak-coupled situation.

6. Controllable formation of multi-core droplets

As we have found in figure 11, compound droplets with a single core inside a shell can be produced precisely within the frequency range in which the inner and outer jets both exhibit synchronized breakup with external actuation. In this section we extend our study to investigate the formation of compound droplets with a controlled number of cores. In previous experiments of Bocanegra *et al.* (2005), they successfully controlled the core numbers to seven through adding a pulse with a large amplitude every seven periods. Following their strategy, we bring in the pulse on the flow rate actuation and examine the production of a compound droplet with controllable cores. Figure 19(a) shows the
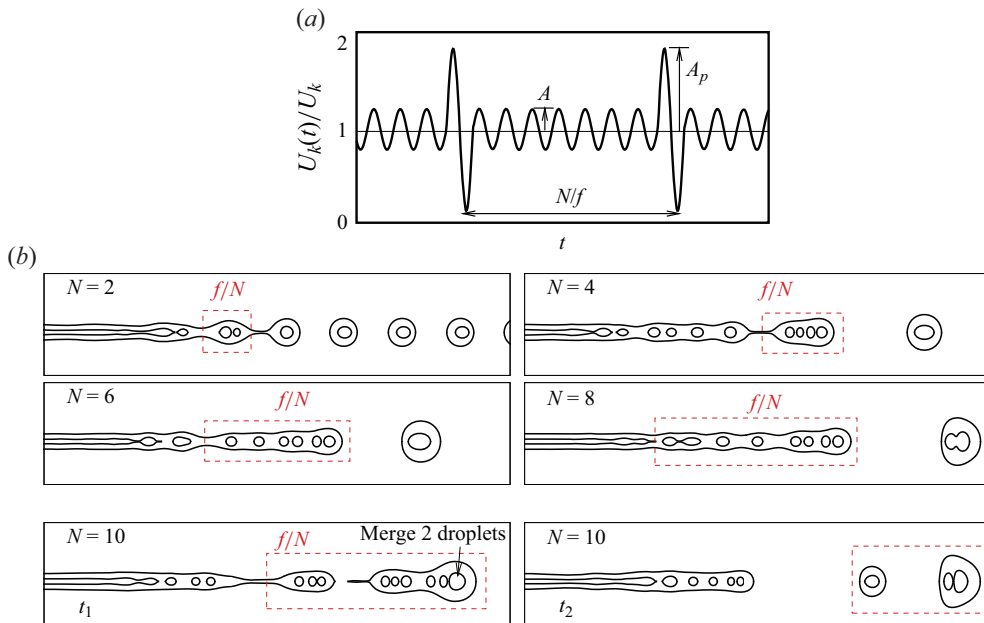
977 A14-28

Figure 19. (*a*) Sketch of the perturbation wave with pulse every N periods. (*b*) Breakup of the weak-coupled coaxial jet ($r_Q = 0.1$) under different N at $f = 70$, $A = 0.1$ and $A_p = 4A$.

sketch of the perturbation wave with a pulse every N period, and the amplitude of the pulse is denoted by A_p. The jet breakup profiles under $f = 70$, $A = 0.1$, $A_p = 4A = 0.4$ but different N are given in figure 19(*b*), respectively. Our results indicate that at a relatively small N (e.g. $N = 2, 4, 6$ and 8), uniform compound droplets with N cores inside can be successfully produced, which is similar to the approach adopted by Bocanegra *et al.* (2005). The generation of compound droplets obeys a working frequency of f/N. Therefore, the size of compound droplets increases as N increases. However, at relatively large N (e.g. $N = 10$), the compound droplets cannot maintain uniformity in size. Instead, the production of compound droplets follows the multiple breakup (M) mode, where two droplets are generated in a working frequency f/N. The mechanism for the occurrence of the M mode as N gradually increases can be explained through comparing the working frequency f/N with the synchronized frequency region of the outer jet. For the liquid flow rates we consider here ($Re = 32.7$, $r_{Q1} + r_{Q2} = 0.0714$ and $r_Q = 0.1$), figure 15(*c,d*) indicates the synchronized frequency region of the outer jet, which is $f = 9$–37 under constant perturbation amplitude $A = 0.1$. When the pulse is added on the flow, the working frequency corresponds to $f/N = 35, 17.5, 11.7$ and 8.8 as $N = 2, 4, 6$ and 8, respectively. As the values of working frequency are almost completely located within the synchronized frequency range of the outer jet, the outer jet is able to present a synchronized breakup manner with uniform compound droplets generated. However, as N increases to 10, the working frequency corresponds to $f/N = 7$, which is obviously lower than the critical frequency for the synchronized breakup of the outer jet; thus, the outer jet presents the M mode with multiple droplets generated in one period. Overall, we can conclude that the method of adding pulse is most suitable for the situation when the frequency f/N locates within the synchronized frequency region of the outer jet.

7. Conclusions

We study the interfacial flow and instability of a coaxial liquid jet in CFF upon actuation through direct numerical simulations by solving the Navier–Stokes equations coupled with a diffuse interface method. Synchronized actuations on the flow rates of core and shell liquids are applied to modulate the flow, and the effects of perturbation frequency, amplitude and liquid flow rates on the evolution of coaxial liquid cones and jets are investigated. The coaxial cone can serve as a reservoir that modulates the external perturbation of the jet. An increase of perturbation amplitude and a decrease of perturbation frequency can increase the local perturbation amplitude of the jet. The coaxial cone can also destabilize at a large perturbation amplitude and small frequency, recoiling upstream of the orifice with intermittent jet behaviour. The relative flow rate between the inner jet and the coaxial jet (denoted by r_Q) plays a significant role on the coupling manner of double interfaces, which has a huge impact on the response modes of jet breakup under external actuation. The effects of perturbation frequency, amplitude and flow rates of core, shell and focusing liquid on the jet breakup modes are studied. It is found that the breakup modes of a weak-coupled jet at small r_Q are much more complicated than those of a strong-coupled jet at large r_Q. Within some frequency range, the breakup of inner and outer jets can be synchronized with external actuation, producing single-encapsulated compound droplets with uniform size. The size of compound droplets can be adjusted by the variation of frequency. The natural frequency of jet breakup locates within the frequency range of the synchronized breakup region. The coaxial jets under weak and strong coupling behaviours are simplified to single jet models, respectively. The scaling analysis and linear instability analysis on these single jet models are carried out, which predict the variation tendency of jet breakup length with actuation amplitude and the natural frequency and the critical frequency for the synchronized breakup region. Furthermore, a strong pulse is added on the perturbation waveform, and the number of cores inside the compound droplets can be precisely controlled through changing the period of the pulse. The critical condition for the feasibility of this strategy is also indicated through comparing the working frequency with the lower critical frequency of the synchronized region. Overall, this numerical investigation can provide guidance for experimental study on active CFF, which is supposed to contribute to the on-demand compound droplets generation in many practical applications.

Declaration of interests. The authors report no conflict of interest.

Author ORCIDs.
- Kai Mu https://orcid.org/0000-0002-4743-2332;
- Ran Qiao https://orcid.org/0000-0002-4445-1255;
- Hang Ding https://orcid.org/0000-0002-7395-6332;
- Ting Si https://orcid.org/0000-0001-9071-8646.

Appendix A. Equations for linear instability analysis

The motion of the liquid jet is governed by the dimensionless Navier–Stokes equations,

$$\nabla \cdot \boldsymbol{u}_i = 0, \tag{A1}$$

$$\rho_i \left(\frac{\partial \boldsymbol{u}_i}{\partial t} + \boldsymbol{u}_i \cdot \nabla \boldsymbol{u}_i \right) = -\nabla p_i + \frac{1}{Re_i} \nabla^2 \boldsymbol{u}_i, \tag{A2}$$

where $\boldsymbol{u}_i$, ρ_i and p_i stand for the velocity, density and pressure and the subscripts $i = 1$ and 2 denote the liquid jet and the surrounding liquid, respectively; and the Reynolds number $Re_1 = Re_t$, $Re_2 = Re_t \cdot S/N$. It is notable that in numerical simulations, the surface tension force is treated as a body force that is contained in the Navier–Stokes equation (see (2.4)); while in linear instability analysis, the influence of surface tension is considered in the boundary condition at the interface. The boundary conditions will be given later.

The normal mode method is utilized for the instability analysis, in which all the variables such as velocity $\boldsymbol{u}_i(r, t)$, pressure $p_i(r, t)$ and interface position $r_j(r, t)$ are split into a basic quantity and a perturbation part,

$$\boldsymbol{u}_i = \boldsymbol{U}_i + \tilde{\boldsymbol{u}}_i, \quad p_i = P_i + \tilde{p}_i, \quad r_j = 1 + \tilde{\eta}, \tag{A3a–c}$$

in which the perturbation part $(\tilde{\boldsymbol{u}}_i, \tilde{p}_i, \tilde{\eta})$ can be expressed in the Fourier form of $\mathrm{e}^{\mathrm{i}(kz-\omega t)}$ in the cylindrical coordinates (r, z), i.e.

$$\tilde{\boldsymbol{u}}_i = (\hat{u}_i(r), \hat{v}_i(r)) \, \mathrm{e}^{\mathrm{i}(kz-\omega t)}, \quad \tilde{p}_i = \hat{p}_i(r) \, \mathrm{e}^{\mathrm{i}(kz-\omega t)}, \quad \tilde{\eta} = \eta \, \mathrm{e}^{\mathrm{i}(kz-\omega t)}, \tag{A4a–c}$$

where $\hat{u}_i(r)$ and $\hat{v}_i(r)$ are the amplitude of velocity perturbation in the z and r directions, respectively. Here $\hat{p}_i(r)$ is the amplitude of pressure perturbations and η is the perturbation amplitudes on the jet interface, respectively; k is the dimensionless wavenumber, which is the reciprocal of the axial perturbation wavelength λ, $\omega = \omega_r + \mathrm{i}\omega_i$ is the dimensionless complex frequency, where ω_i denotes the growth rate of perturbations.

The perturbations of all quantities are assumed to be very small, which allows us to expand the Navier–Stokes equations and only keep the first-order perturbation terms. Therefore, substituting these perturbations into the governing equations and neglecting the high-order terms, we can get the linearized governing equations,

$$\frac{\mathrm{d}\hat{v}_i}{\mathrm{d}r} + \frac{\hat{v}_i}{r} + \mathrm{i}k\hat{u}_i = 0, \tag{A5}$$

$$\frac{1}{Re_i} \left[\frac{\mathrm{d}^2\hat{v}_i}{\mathrm{d}r^2} + \frac{1}{r}\frac{\mathrm{d}\hat{v}_i}{\mathrm{d}r} - \left(k^2 + \frac{1}{r^2} + \mathrm{i}kRe_iU_i \right) \hat{v}_i \right] - \left(\frac{1}{S} \right)^{\delta_{i2}} \frac{\mathrm{d}\hat{p}_i}{\mathrm{d}r} + \mathrm{i}\omega\hat{v}_i = 0, \tag{A6}$$

$$\frac{1}{Re_i} \left[\frac{\mathrm{d}^2\hat{u}_i}{\mathrm{d}r^2} + \frac{1}{r}\frac{\mathrm{d}\hat{u}_i}{\mathrm{d}r} - (k^2 + \mathrm{i}kRe_iU_i)\hat{u}_i \right] - \frac{\mathrm{d}U_i}{\mathrm{d}r}\hat{v}_i - \left(\frac{1}{S} \right)^{\delta_{i2}} \mathrm{i}k\hat{p}_i + \mathrm{i}\omega\hat{u}_i = 0. \tag{A7}$$

The velocity and the pressure at the symmetry axis should satisfy the consistency conditions

$$\hat{v}_1 = \frac{\mathrm{d}\hat{u}_1}{\mathrm{d}r} = \frac{\mathrm{d}\hat{p}_1}{\mathrm{d}r} = 0. \tag{A8}$$

At the interface $r_j = 1 + \eta \, \mathrm{e}^{\mathrm{i}(kz-\omega t)}$, the continuity of velocity, the kinematic boundary condition and the force balance on the tangential and normal directions should be satisfied, i.e.

$$\hat{v}_1 = \hat{v}_2, \quad \hat{u}_1 + \frac{\mathrm{d}U_1}{\mathrm{d}r}\eta = \hat{u}_2 + \frac{\mathrm{d}U_2}{\mathrm{d}r}\eta, \tag{A9}$$

$$-\mathrm{i}\omega\eta = \hat{v}_j - \mathrm{i}kU_1\eta, \tag{A10}$$

$$\hat{p}_2 - \frac{2N}{Re}\frac{\mathrm{d}\hat{v}_2}{\mathrm{d}r} - \hat{p}_1 - \frac{2}{Re}\frac{\mathrm{d}\hat{v}_1}{\mathrm{d}r} = \frac{1}{We}(1 - k^2)\eta, \tag{A11}$$

$$\mathrm{i}k\hat{v}_1 + \frac{\mathrm{d}\hat{u}_1}{\mathrm{d}r} + \frac{\mathrm{d}^2U_1}{\mathrm{d}r^2}\eta = N \left(\mathrm{i}k\hat{v}_2 + \frac{\mathrm{d}\hat{u}_2}{\mathrm{d}r} + \frac{\mathrm{d}^2U_2}{\mathrm{d}r^2}\eta \right). \tag{A12}$$

The infinity boundary condition at $r \to \infty$ is

$$\hat{v}_2 = \frac{\mathrm{d}\hat{u}_2}{\mathrm{d}r} = \frac{\mathrm{d}\hat{p}_2}{\mathrm{d}r} = 0. \tag{A13}$$

In the calculation, this condition can be satisfied by employing a finite and sufficiently large distance.

The governing equations and the boundary conditions form an eigenvalue problem. The Chebyshev spectral collocation method has been utilized to solve the problem, in which a Matlab code was successfully developed (Si *et al.* 2009).

REFERENCES

ANNA, S.L. 2016 Droplets and bubbles in microfluidic devices. *Annu. Rev. Fluid Mech.* **48**, 285–309.

BARRERO, A. & LOSCERTALES, I.G. 2007 Micro- and nanoparticles via capillary flows. *Annu. Rev. Fluid Mech.* **39**, 89–106.

BASARAN, O.A., GAO, H.J. & BHAT, P.P. 2013 Nonstandard inkjets. *Annu. Rev. Fluid Mech.* **45**, 85–113.

BOCANEGRA, R., SAMPEDRO, J.L., GAÑÁN-CALVO, A.M. & MARQUEZ, M. 2005 Monodisperse structured multi-vesicle microencapsulation using flow-focusing and controlled disturbance. *J. Microencapsul.* **22**, 745–759.

CHAUHAN, A., MALDARELLI, C., PAPAGEORGIOU, D.T. & RUMSCHITZKI, D.S. 2000 Temporal instability of compound threads and jets. *J. Fluid Mech.* **420**, 1–25.

CHEN, J.N. & LIN, S.P. 2002 Instability of an annular jet surrounded by a viscous gas in a pipe. *J. Fluid Mech.* **450**, 235–258.

CHEN, L., YANG, C., XIAO, Y., YAN, X., HU, L., EGGERSDORFER, M., CHEN, D., WEITZ, D.A. & YE, F. 2021 Millifluidics, microfluidics, and nanofluidics: manipulating fluids at varying length scales. *Mater. Today Nano* **16**, 100136.

CRASTER, R.V., MATAR, O.K. & PAPAGEORGIOU, D.T. 2005 On compound liquid threads with large viscosity contrasts. *J. Fluid Mech.* **533**, 95–124.

DING, H., SPELT, P.D.M. & SHU, C. 2007 Diffuse interface model for incompressible two-phase flows with large density ratios. *J. Comput. Phys.* **226**, 2078–2095.

EGGERS, J. 1997 Nonlinear dynamics and breakup of free-surface flows. *Rev. Mod. Phys.* **69**, 3.

EGGERS, J. & VILLERMAUX, E. 2008 Physics of liquid jets. *Rep. Prog. Phys.* **71**, 036601.

EVANGELIO, A., CAMPO-CORTES, F. & GORDILLO, J.M. 2016 Simple and double microemulsions via the capillary breakup of highly stretched liquid jets. *J. Fluid Mech.* **804**, 550–577.

GAÑÁN-CALVO, A.M. 1998 Generation of steady liquid microthreads and micron-sized monodisperse sprays in gas streams. *Phys. Rev. Lett.* **80**, 285–288.

GAÑÁN-CALVO, A.M., GONZALEZ-PRIETO, R., RIESCO-CHUECA, P., HERRADA, M.A. & FLORES-MOSQUERA, M. 2007 Focusing capillary jets close to the continuum limit. *Nat. Phys.* **3**, 737–742.

GAÑÁN-CALVO, A.M. & MONTANERO, J.M. 2009 Revision of capillary cone-jet physics: electrospray and flow focusing. *Phys. Rev.* E **79**, 066305.

GAÑÁN-CALVO, A.M., MONTANERO, J.M., MARTIN-BANDERAS, L. & FLORES-MOSQUERA, M. 2013 Building functional materials for health care and pharmacy from microfluidic principles and flow focusing. *Adv. Drug Deliv. Rev.* **65**, 1447–1469.

GAÑÁN-CALVO, A.M. & RIESCO-CHUECA, P. 2006 Jetting-dripping transition of a liquid jet in a lower viscosity co-flowing immiscible liquid: the minimum flow rate in flow focusing. *J. Fluid Mech.* **553**, 75–84.

GUERRERO, J., CHANG, Y.W., FRAGKOPOULOS, A.A. & FERNANDEZ-NIEVES, A. 2020 Capillary-based microfluidics-coflow, flow-focusing, electro-coflow, drops, jets, and instabilities. *Small* **16**, 1904344.

HERRADA, M.A., GAÑÁN-CALVO, A.M. & OJEDA-MONGE, A. 2008 Liquid flow focused by a gas: jetting, dripping, and recirculation. *Phys. Rev.* E **78**, 036323.

HERRADA, M.A., MONTANERO, J.M., FERRERA, C. & GAÑÁN-CALVO, A.M. 2010 Analysis of the dripping-jetting transition in compound capillary jets. *J. Fluid Mech.* **649**, 523–536.

JACQMIN, D. 1999 Calculation of two-phase Navier-Stokes flows using phase-field modeling. *J. Comput. Phys.* **155**, 96–127.

KAMIS, Y.E., ERAL, H.B. & BREUGEM, W.P. 2021 Active control of jet breakup and droplet formation using temperature modulation. *Phys. Rev. Fluids* **6**, 103903.

LIN, S.P. 2003 *Breakup of Liquid Sheets and Jets*. Cambridge University Press.

LIU, H., WANG, Z., GAO, L., HUANG, Y., TANG, H., ZHAO, X. & DENG, W. 2021 Optofluidic resonance of a transparent liquid jet excited by a continuous wave laser. *Phys. Rev. Lett.* **127**, 244502.

LIU, X.D., WU, L.Y., ZHAO, Y.J. & CHEN, C.Y. 2017 Study of compound drop formation in axisymmetric microfluidic devices with different geometries. *Colloid Surf.* A **533**, 87–98.

LIU, Z.M., WANG, J., PANG, Y., ZHOU, Q. & LI, M.Q. 2020 Role of periodic inner dripping on compound jets in a capillary device. *Intl J. Multiphase Flow* **123**, 103180.

LUO, J., LYU, S.N., QI, L.H. & LI, N. 2023 Generation of the small tin-droplet streams with a manipulable droplet spacing via the forced velocity perturbation. *Phys. Fluids* **35**, 013612.

MAGALETTI, F., FRANCESCO, P., CHINAPPI, M., MARINO, L. & CASCIOLA, C.M. 2013 The sharp-interface limit of the Cahn–Hilliard/Navier–Stokes model for binary fluids. *J. Fluid Mech.* **714**, 95–126.

MOALLEMI, N., LI, R. & MEHRAVARAN, K. 2016 Breakup of capillary jets with different disturbances. *Phys. Fluids* **28**, 012101.

MU, K., DING, H. & SI, T. 2018*a* Instability analysis of the cone-jet flow in liquid-driven flow focusing. *Microfluid Nanofluid* **22**, 138.

MU, K., DING, H. & SI, T. 2020*a* Experimental and numerical investigations on interface coupling of coaxial liquid jets in co-flow focusing. *Phys. Fluids* **32**, 042103.

MU, K., LI, G.B. & SI, T. 2020*b* Instability and interface coupling of coaxial liquid jets in a driving stream. *Phys. Fluids* **32**, 092107.

MU, K., QIAO, R., GUO, J.F., YANG, C.Y., WU, Y.F. & SI, T. 2021*a* Parametric study on stability and morphology of liquid cone in flow focusing. *Intl J. Multiphase Flow* **135**, 103507.

MU, K., QIAO, R., SI, T., CHEN, X.Q. & DING, H. 2021*b* Interfacial instability and transition of jetting and dripping modes in a co-flow focusing process. *Phys. Fluids* **33**, 052118.

MU, K., SI, T. & DING, H. 2019 Nonlinear dynamics and manipulation of dripping in capillary flow focusing. *Sci. China Phys. Mech.* **62**, 124713.

MU, K., SI, T., LI, E.Q., XU, R.X. & DING, H. 2018*b* Numerical study on droplet generation in axisymmetric flow focusing upon actuation. *Phys. Fluids* **30**, 012111.

MU, K., ZHANG, C.Y., SI, T. & DING, H. 2022 Experimental and numerical investigations on characteristics of coaxial liquid cone in coflow focusing. *Phys. Rev. Fluids* **7**, 024001.

SHE, L., FANG, Y.S., HU, L., SU, R. & FU, X. 2022 Timing jitter of monodisperse droplets generated by capillary jet breakup. *Phys. Fluids* **34**, 042107.

SI, T., LI, F., YIN, X.Y. & YIN, X.Z. 2009 Modes in flow focusing and instability of coaxial liquid-gas jets. *J. Fluid Mech.* **629**, 1–23.

VLADISAVLJEVIĆ, G.T., NUUMANI, R.A. & NABAVI, S.A. 2017 Microfluidic production of multiple emulsions. *Micromachines* **8**, 75.

WANG, N.N., SEMPREBON, C., LIU, H.H., ZHANG, C.H. & KUSUMAATMAJA, H. 2020 Modelling double emulsion formation in planar flow-focusing microchannels. *J. Fluid Mech.* **895**, A22.

XU, C.H., HE, W.Q., YANG, W.W., DENG, W.W. & XIA, H.H. 2022*a* Controlling instabilities of electrified liquid jets via orthogonal perturbations. *Phys. Rev. Fluids* **7**, 043702.

XU, X., ZHU, Z.Q., MU, K., HUANG, F.S. & SI, T. 2022*b* Parametric study on breakup of liquid jet in a gas-driven flow focusing process upon external excitation. *Phys. Fluids* **34**, 042001.

YANG, C.Y., QIAO, R., MU, K., ZHU, Z.Q., XU, R.X. & SI, T. 2019 Manipulation of jet breakup length and droplet size in axisymmetric flow focusing upon actuation. *Phys. Fluids* **31**, 091702.

YANG, W., DUAN, H., LI, C. & DENG, W. 2014 Crossover of varicose and whipping instabilities in electrified microjets. *Phys. Rev. Lett.* **112**, 054501.

ZHANG, T.X., ZHOU, X., XU, L., PAN, D.W. & HUANG, W.X. 2021 Numerical investigation of fluid property effects on formation dynamics of millimeter-scale compound droplets in a co-flowing device. *Chem. Engng Sci.* **229**, 116156.

ZHAO, Y., WAN, D.M., CHEN, X.L., CHAO, X. & XU, H.T. 2021 Uniform breaking of liquid-jets by modulated laser heating. *Phys. Fluids* **33**, 044115.

ZHU, P.A. & WANG, L.Q. 2022 Microfluidics-enabled soft manufacture of materials with tailorable wettability. *Chem. Rev.* **122**, 7010–7060.